University of Zululand

A High Precision Branching Ratio Measurement In ^{19}Ne Beta Decay

By

Phumzile Z. Mabika

A thesis submitted in partial fulfillment
of the requirement for the degree of

Master of Science
(Physics)

Supervisor:

Dr. S.S. Ntshangase

University of Zululand

Co-Supervisor:

Prof. S. Triambak

University of the Western Cape

University of Zululand

2017

Declaration

I declare that the work contained in this thesis is my own work and it has not been submitted for any degree or examination in any other university, and that all sources I have used or quoted have been indicated and acknowledged by complete references.

Phumzile Zandile Mabika   May 2017

Signature:

I dedicate this thesis to my loving mother.

Acknowledgements

Abstract

This thesis describes the analysis of data from a ^{19}Ne beta decay experiment with a radioactive ^{19}Ne beam to obtain a measurement of the β decay branching ratio to the $1/2^+$ ground state in ^{19}F. This measurement will determine the ft value (comparative half life) of the decay with high accuracy and precision. Together with a previously measured beta asymmetry parameter (A_β) for ^{19}Ne beta decay, our measured ft value, which is corrected for nuclear structure and radiative effects ($\mathcal{F}t^{^{19}\text{Ne}}$=1720.0±1.3 s), can be used to place bounds on predicted right-handed weak interactions, beyond the current Standard Model of particle physics.

Contents

List of Figures

iv

List of Tables

Chapter 1

Introduction

The belief that the universe is constructed of fundamental (tiny and indivisible) particles has been around since the ancient Greeks. During the early 1800s, atoms were assumed to be fundamental building blocks of matter. It was only after around 100 years or so that experimental evidence showed atoms can be broken into smaller constituents such as protons, neutrons and electrons. Our present knowledge tells us that protons and neutrons are themselves made of quarks, which are believed to be elementary particles.

Based on our current theoretical and experimental understanding, elementary particles and the interactions between them are described by the Standard Model (SM) of particle physics, a theoretical model that describes matter at the smallest scales. The SM was developed to its present form during the 1950s and 1970s [1]. Within the SM, fundamental particles comprise six quarks (up, down, strange, charm, top and bottom) and six leptons (electron, electron neutrino, muon, muon neutrino, tau and tau neutrino). These particles have half-integer spin (are fermions). Three of the four known interactions (strong, weak and electromagnetic) are described in the SM by the exchange of bosons (integral spin particles). The fourth (gravity) is left out, as one of the biggest challenges in theoretical physics today is to have a satisfactory quantum mechanical description that includes the gravitational interaction in the model.

Figure 1.1 classifies the known elementary particles and fundamental interactions within the Standard Model. The newest addition to the list is the Higgs boson, which was discovered at the Large Hadron Collider (LHC) in 2012. Unlike the other gauge bosons, the Higgs is a spin-0 boson (scalar) and is responsible for giving the W and Z bosons (amongst other particles) their mass.
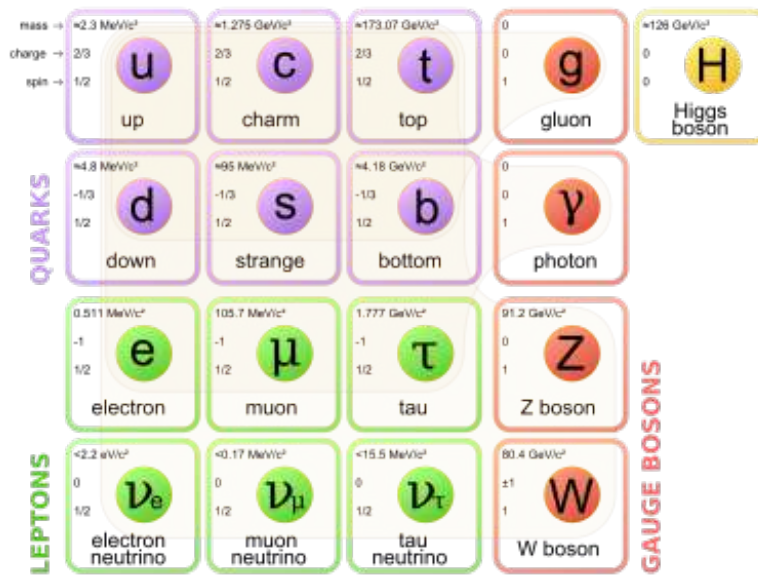
Figure 1.1: Classification of fundamental particles and interactions in the Standard Model.

Over the past several decades, with the advent of high energy colliders, the Standard Model has seen tremendous success. For example it correctly predicted the existence of the top quark, and the masses of the $W^{\pm}$ and Z^0 bosons and the Higgs boson [5]. Furthermore, the SM also was successful in unifying the electromagnetic and weak interactions in a standard 'electroweak' theory. The only modification to the originally proposed SM, after more than four decades of research is that neutrinos, which were previously assumed to be massless, are now known to be massive [6]. Despite this success, it is widely believed that the SM does not describe a complete picture of fundamental particles and interactions, as many of the ingredients in the

2

model were introduced due to experimental evidence alone. For example, some features in weak decays, such parity and CP-violation are not natural consequences of the model. As a result there is currently a lot of interest in the global physics community to look for physics beyond the SM (BSM). Experimentally, the searches for BSM physics are pursued using three broad approaches:

1. Using high energy collider experiments.

2. Using low-background deep underground experiments.

3. Via precision tests of the fundamental symmetries that are assumed in the model.

This thesis describes the analysis of data that pertains to the third category. In particular this work is relevant for stringent tests of the $V - A$ (vector, minus axial vector) structure of the weak interactions that forms an important foundation of the standard electroweak theory. The weak interaction current is currently assumed to have no right-handed, scalar or tensor currents. This assumption is based on experiment, as there is no fundamental principle that forbids the existence of non $V - A$ currents. In fact, several theoretical extensions to the SM allow the exchange of massive exotic particles that could have right-handed, scalar or tensor contributions [7]. However there have been no direct or indirect experimental signatures of such exotic couplings to date. Precise measurements of observables such as decay rates and angular correlations in nuclear beta decays can be used to stringently test the assumed symmetries in the SM to probe for these exotic couplings, beyond the established $V - A$ picture of weak interactions. One such probe is a measurement of the beta asymmetry (A_β) from the decays of spin-polarized nuclei. In such experiments, the distribution of the emitted beta particles (as it is virtually impossible to detect neutrinos), relative to the polarization of the parent nucleus can be used to probe for right-handed ($V + A$ type) weak interactions [7]. In this regard, the beta asymmetry in ^{19}Ne beta decay offers an enhanced sensitivity for such searches [8]. In order to meaningfully place bounds on right-handed currents from nuclear β decays, one needs a precise

3

measurement of the β decay rate in addition to the β asymmetry [9, 10]. The β asymmetry in ^{19}Ne β decay has already been measured with a reasonably high precision [11] to be $A_\beta = (-3.91 \pm 0.14)\%$.
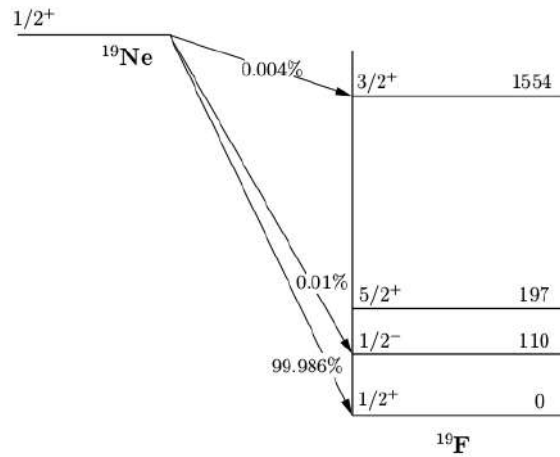
Figure 1.2: The β-decay scheme for ^{19}Ne.

In this thesis we describe analysis of data to obtain the comparative half life (ft value) for ^{19}Ne β decay, which, together with the measured β asymmetry forms part of a useful data-set for searches of right-handed weak interactions. The β decay scheme for ^{19}Ne is shown in figure 1.2. For the ft value, one requires measurements of the half-life of ^{19}Ne, the $\frac{1}{2}^+ \rightarrow \frac{1}{2}^+$ branching ratio and the Q value for the decay. This thesis describes experimental work to obtain the branching ratio for the decay of ^{19}Ne to the ground state in ^{19}F. The result will be used to obtain the ft value of the decay for searches of right-handed currents using ^{19}Ne β decay.

Chapter 2

Weak Interactions And The Standard Model

2.1 The Fundamental Forces

In essence there are four known forces that govern physical processes in nature, namely: gravitational, electromagnetic, strong and weak interactions. These forces are considered fundamental because all physical processes can be traced back to either one or a combination of them. They have different ranges as well as unequal strengths.

Table 2.1: The four fundamental interactions [3]

Type	Range	Relative Strength	Typical Particle
Strong	1 fm	1	π, K, n, p
Electromagnetic	∞	10^{-2}	e, μ, π, K, p
Weak	10^{-3} fm	10^{-7}	ν_e, τ, μ
Gravity	∞	10^{-38}	all

Table 2.1 lists the known forces in decreasing order of their strength. The strong force is short ranged and only effective at scales of $\approx 10^{-15}$ m. It is the force that holds atomic nuclei together against the strong repulsion of the protons resulting from their charge.

The electromagnetic force on the other hand has infinite range and it plays an important role within the atom. It affects only charged particles and competes with the strong force within nuclei in determining nuclear properties. The weak interaction has the shortest range of them all and it plays a significant role in nuclear beta decays and other weakly interacting processes such as muon decays and neutrino-nucleus interactions etc. Due to the lack of an adequate quantum mechanical description of gravity for subatomic systems, we exclude gravity in our discussion.

Fundamental interactions can be described by the exchange of virtual particles called gauge bosons. These force carrier particles are said to be virtual because they exist for a very short time. As an example, the Coulomb interaction between two charged particles is associated with a virtual exchange of photons between the particles and these photons couple to the electric charge. The theory of quantum electrodynamics (QED) is borne from this type of interaction [1]. Similarly, in strong and weak interactions the forces are mediated via the exchange of gluons and the W and Z bosons. The W and Z bosons have masses of roughly 80 GeV and 90 GeV respectively, and are listed in figure 1.1. In this chapter I limit my discussion to the weak interactions, which is relevant for this thesis.

2.2 The Weak Interactions

Weak interactions play an important role in understanding the behaviour of the fundamental particles as well as the evolution of the universe. Usually weakly interacting processes are slow in comparison with strong or electromagnetic interactions. As mentioned previously, this type of interaction is associated with massive spin-1 vector bosons that act as force carrier particles. The short range of weak interactions is a result of the exchange of these massive bosons. At low energies weak interactions are referred to as point or zero-range interactions. Figure 2.1 depicts examples of Feynman diagrams for neutral and charged weak interactions, which occur by the exchange of massive Z and W bosons respectively [1].

(a) An example of a neutral weak current interaction

(b) An example of a charged weak current interaction
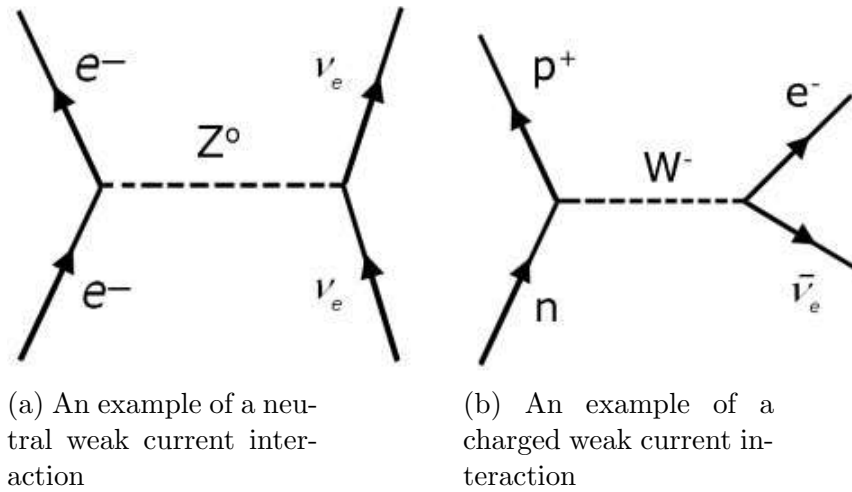
Figure 2.1: Examples of Feynman diagrams for weak interactions mediated by neutral and charged currents respectively [1].

The charged weak interaction processes can be classified as purely leptonic, purely hadronic, or semi-leptonic. Some examples of these processes are:

- Leptonic muon decay : $\mu^- \rightarrow e^- + \bar{\nu}_e + \nu_\mu$

- Hadronic lambda decay : $\Lambda^0 \rightarrow \pi^- + p$

- Semi-leptonic neutron decay : $n \rightarrow p + e^- + \bar{\nu}_e$

The strength of weak interactions is characterized by a *universal* Fermi coupling constant $G_F = 1.66 \times 10^{-5}$ GeV^{-2} [12]. In what follows below, I describe nuclear β decays, which are semi-leptonic weak interaction processes.

2.2.1 Nuclear beta decays

A nuclear beta decay is a process in which one nucleus decays to another one with the atomic number incremented or decremented by one unit. Such a process is accompanied by the emission of two leptons. There are three types of beta decays [3]:

1. β^- decay: ${}^A_Z X_N \rightarrow {}^A_{Z+1} X'_{N-1} + e^- + \bar{\nu}_e$

7

2. β^+ decay: $^A_Z X_N \rightarrow^A_{Z-1} X'_{N+1} + e^+ + \nu_e$

3. Electron capture : $^A_Z X_N + e^- \rightarrow^A_{Z-1} X'_{N+1} + \nu_e$

Unlike α or γ decays, the spectrum of β particles following β decays have a continuous energy spectrum as shown in figure 2.2. This is because in β decays the emitted $e^\pm$ particle is also accompanied by the $\nu_e(\bar{\nu}_e)$ which shares the energy available from the decay. The (anti) neutrinos are highly penetrating leptons that are very difficult to detect. Let us consider a neutron (β^-) decay:

$n \rightarrow p + e^- + \bar{\nu}_e$.

(a) Alpha decay spectrum   (b) Beta decay spectrum.
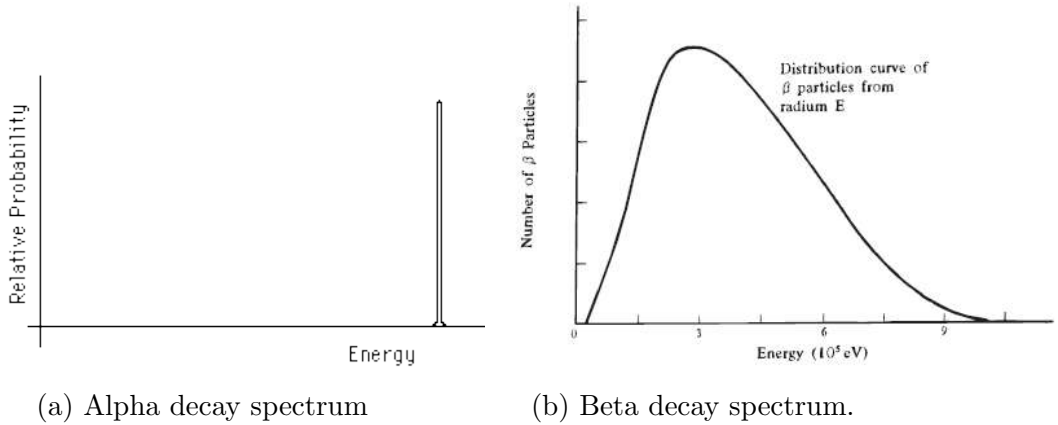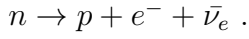
Figure 2.2: The qualitative difference between α and β decay spectra. The maximum energy carried by the β particles is called the end point energy of the decay [2].

The Q value for this decay is

$$Q_{\beta^-} = (m_n - m_p)c^2, \qquad (2.1)$$

which determines the energy released during the decay process [3]. If one assumes the recoil is negligible, the energy is shared between the neutrino and electron.

$$Q_{\beta^-} = E_{\nu_e} + E_e. \qquad (2.2)$$

The total energy of the electron in a neutron decay is given by

$$E_e = T_e + m_e c^2. \tag{2.3}$$

where T_e is the kinetic energy. The same formalism applies for nuclear β decays. In terms of atomic masses, for nuclear β decays the Q values are as follows

- β^- decay : $Q_{\beta^-} = [M(Z, A) - M(Z + 1, A)]$

- β^+ decay : $Q_{\beta^+} = [M(Z, A) - M(Z - 1, A)] - 2m_e c^2$

- EC decay : $Q_{EC} = [M(Z, A) - M(Z - 1, A)] - BE,$

where BE is the binding energy of the captured inner shell electron.

In the discussion that follows, I use the terms electrons for both electrons and positrons, and neutrinos for both neutrinos and anti-neutrinos. A nuclear β decay transition rate can be obtained using pertubation theory, assuming the transition is caused by the charged weak interaction. The decay rate is expressed as

$$\lambda = \frac{1}{\tau} = \frac{2\pi}{\hbar} |V_{fi}|^2 \rho(E_f), \tag{2.4}$$

where τ is the lifetime of the initial state. The above equation is called Fermi's Golden Rule [3]. Other than the constant, the right-hand side consists of two parts: *the matrix element*, which contains the operator responsible for the transition and *the density of the final states* which statistically represents the phase space available for the decay. These two parts will be looked at separately below.

The matrix element

The matrix element in equation (2.4), connecting the initial and final state of the system can be written as

$$V_{fi} = \int \psi_f^* \hat{O} \psi_i d^3 r, \tag{2.5}$$

where $\hat{O}$ is the operator responsible for the decay. The final state wave function ψ_f is actually a product of lepton and the daughter wave functions, such that

$$V_{fi} = g \int \psi_f^* \psi_e^* \psi_{\nu_e}^* \hat{O} \psi_i d^3 r, \qquad (2.6)$$

where g represents the weak interaction coupling constant, $\psi_f^* \psi_e^* \psi_{\nu_e}^*$ are the daughter nucleus, electron and neutrino wave functions respectively and ψ_i is the wave function of the parent nucleus in the initial state. The lepton wave functions can be represented by plane waves which are normalized to unit volume as follows:

$$\psi_e(r) = \frac{1}{\sqrt{V}} e^{\frac{i\vec{p}_e \cdot \vec{r}}{\hbar}} \qquad \text{and} \qquad \psi_{\nu_e}(r) = \frac{1}{\sqrt{V}} e^{\frac{i\vec{p}_{\nu_e} \cdot \vec{r}}{\hbar}}. \qquad (2.7)$$

Within the *allowed approximation* for nuclear β decays, $pr << 1$, both the leptonic wave functions reduce to

$$e^{\frac{i\vec{p} \cdot \vec{r}}{\hbar}} = 1 + \frac{i\vec{p} \cdot \vec{r}}{\hbar} + \frac{1}{2} \left(\frac{i\vec{p} \cdot \vec{r}}{\hbar} \right)^2 + \cdots \cong 1, \qquad (2.8)$$

$$\Rightarrow \psi_e(\vec{r}) = \frac{1}{\sqrt{V}} \qquad \text{and} \qquad \psi_{\nu_e}(\vec{r}) = \frac{1}{\sqrt{V}}. \qquad (2.9)$$

With these substitutions, equation (2.6) becomes

$$V_{fi} = \frac{g}{V} \int \psi_f^*(\vec{r}) \hat{O} \psi_i(\vec{r}) d^3 r$$
$$V_{fi} = \frac{g}{V} M_{fi}, \qquad (2.10)$$

where $M_{fi} = \int \psi_f^*(\vec{r}) \hat{O} \psi_i(\vec{r}) d^3 r$ is the nuclear matrix element for the β decay.

The density of states

The factor $\rho(E_f)$ in equation (2.4) is the density of the final states available for the decay. It is the number of states available over the energy interval for all possible final states. On labelling the electron or neutrino momenta as p, in momentum space the locus of points having momenta between the values p and $p + dp$ is a spherical shell of volume $4\pi p^2 dp$. Assuming the lepton is

confined in a box of volume V, then the number of final states in the range p and $p + dp$ in 6-dimensional phase space is

$$dn_e = \frac{4\pi p_e^2 dp_e}{h^3} V \qquad \text{and} \qquad dn_{\nu_e} = \frac{4\pi p_{\nu_e}^2 dp_{\nu_e}}{h^3} V \qquad (2.11)$$

where the denominator h^3 serves to make the quantity dimensionless. As they are both produced in the final state, the combined number of states for the decay becomes:

$$d^2n = dn_e dn_{\nu_e} = \frac{(4\pi)^2 V^2 p_e^2 dp_e p_{\nu_e}^2 dp_{\nu_e}}{h^6} \qquad (2.12)$$

Then the density of available states for a given endpoint energy E_f can be written as

$$\rho(E) = (4\pi)^2 V^2 \frac{d}{dE_f} \int_0^{p_{max}} p_e^2 dp_e \frac{(E_f - E_e)^2}{c^2} \cdot \frac{1}{c}, \qquad (2.13)$$

as $E_f \simeq E_e + E_\nu$, and for a fixed E_e and p_e, $p_\nu \simeq \frac{E_\nu}{c}$ for almost massless neutrinos. Evaluating the above integral between the limits $m_e c^2$ and E_f and making the further assumption that for a fixed E_e, $p_e >> m_e c^2 \approx \frac{E_e}{c} \Rightarrow dp_e = \frac{dE_e}{c}$ we obtain

$$\rho(E) = \frac{(4\pi)^2 V^2}{h^6 c^6} \int_{m_e c^2}^{E_f} (E_f - E_e) E_e^2 dE_e \qquad (2.14)$$

$$\text{or} \quad \rho(E) \approx \frac{(4\pi)^2 E_f^5}{h^6 c^6} \cdot \frac{1}{30}, \qquad (2.15)$$

for unit volume. This is called Sargent's rule for β decay. Since the endpoint energy can be directly obtained from the Q value of the decay, the differential decay rate can be obtained from Fermi's Golden rule (equation (2.4))

$$d\lambda = \frac{g^2 |M_{fi}|^2}{2\pi^3 \hbar^7 c^3} p_e^2 (Q_\beta - E_e)^2. \qquad (2.16)$$

From the above we can obtain the number of emitted electrons in the range p_e and $p_e + dp_e$. On absorbing all the factors that do not depend on electron

momentum, into a constant K and further substituting $E_e = \sqrt{p_e^2 c^2 + m_e^4 c^4}$, the number of electrons with momentum p_e reduces to

$$N(p_e) = \frac{K}{c^2} p_e^2 (Q_\beta - \sqrt{p_e^2 c^2 + m_e^4 c^4})^2. \qquad (2.17)$$

This function plays the role of determining the shape of the β spectrum shown in figure 2.3. As shown in the figure, the shapes of β spectra following β^- decay and β^+ decay are markedly dissimilar. This difference is due to the Coulomb barrier of the nucleus that affects the energy distribution of the electrons (positrons).

(a) Electron energy distribution

(b) Positron energy distribution
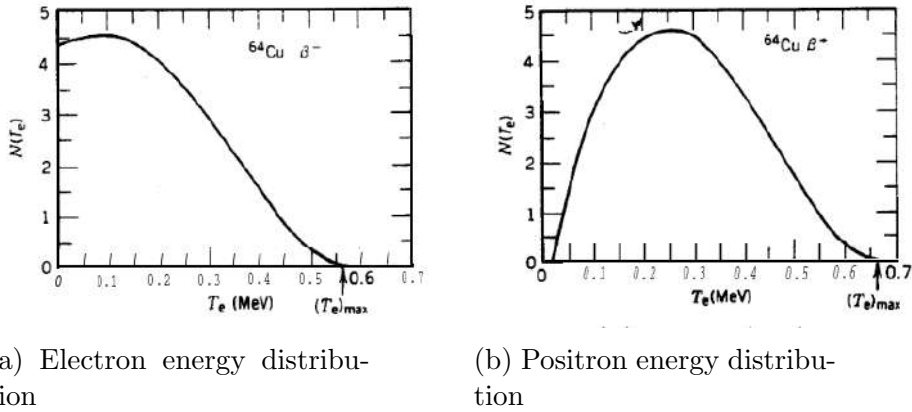
Figure 2.3: Energy distribution of the electrons and positrons in the beta decay of ^{64}Cu [3].

The Coulomb effect between daughter nucleus and charged leptons leads to a significant distortion of the latter's wave functions. To incorporate this effect, the electron (positron) plane wave solution in equation (2.7) should ideally be replaced with a distorted wave function due to Coulomb potential. These calculations are beyond the context of this thesis. The result is the modification of the β spectra by introducing a correction factor, the Fermi function, $F(Z', p_e)$, where Z' is the atomic number of the daughter nucleus and equation (2.17) becomes [3].

$$N(p_e) = \frac{K}{c^2} F(Z', p_e) p_e^2 (Q_\beta - \sqrt{p_e^2 c^2 + m_e^4 c^4})^2. \qquad (2.18)$$

The total decay rate now reduces to

$$\lambda = \frac{g^2|M_{fi}|^2}{2\pi^3\hbar^7c^3} \int\limits_{m_ec^2}^{E_f} F(Z',p_e)p_e^2(E_f - E_c)^2 dE_e, \tag{2.19}$$

$$\text{or} \quad \lambda = \frac{g^2|M_{fi}|^2}{2\pi^3\hbar^7c} m_e^5 \ f(Z',E_e). \tag{2.20}$$

where,

$$f(Z',E_e) = \frac{1}{(m_ec)^3(m_ec^2)^2} \int\limits_{m_ec^2}^{E_f} F(Z',E_e)p_e^2(E_f - E_e)^2 dE_e. \tag{2.21}$$

is the dimensionless phase space factor for the decay [3]. Since the decay rate is given in terms of the half-life as $\lambda = \frac{\ln 2}{t_{1/2}}$, equation (2.20) becomes:

$$ft_{1/2} = \ln 2 \frac{2\pi^3\hbar^7}{g^2m_e^5c^4|M_{fi}|^2}. \tag{2.22}$$

The $ft_{1/2}$ value for a decay is inversely proportional to the matrix element, and called the comparative half life.

2.2.2   Relativistic formulation of β decays

Since the neutrinos and electrons have a very small mass compared to the Q values in nuclear β decays, it is best that the theory be formulated relativistically. Dirac originally proposed a relativistically covariant wave equation to describe the quantum dynamics of spin 1/2 fermions [12]. Both the intrinsic spin of particles and the prediction of the existence of antiparticles were natural consequences of this profound equation, which is put forth as [1]

$$(i\gamma^\mu\partial_\mu - m)\psi = 0, \tag{2.23}$$

where $\hbar = c = 1$ and the index μ runs from 0 to 3. In the above equation the ψ is a 4 component column vector called a Dirac spinor,

$$\psi = \begin{pmatrix} \psi_1 \\ \psi_2 \\ \psi_3 \\ \psi_4 \end{pmatrix}. \tag{2.24}$$

The γ's are a class of 4×4 matrices, called Dirac or γ matrices that satisfy the anti commutation relation

$$\{\gamma^{\mu}, \gamma^{\nu}\} = \gamma^{\mu}\gamma^{\nu} + \gamma^{\nu}\gamma^{\mu} = 2g^{\mu\nu}, \tag{2.25}$$

where $g^{\mu\nu}$ is the metric tensor

$$g^{\mu\nu} = \begin{pmatrix} 1 & 0 & 0 & 0 \\ 0 & -1 & 0 & 0 \\ 0 & 0 & -1 & 0 \\ 0 & 0 & 0 & -1 \end{pmatrix}. \tag{2.26}$$

More precisely, the representation of γ's is as follows:

$$\gamma^0 = \begin{pmatrix} I & O \\ O & -I \end{pmatrix} \qquad \gamma^i = \begin{pmatrix} O & \vec{\sigma} \\ -\vec{\sigma} & O \end{pmatrix} \tag{2.27}$$

where I is a 2×2 identity matrix, O is a 2×2 null matrix and the σ's are Pauli spin matrices

$$\sigma_1 = \begin{pmatrix} 0 & 1 \\ 1 & 0 \end{pmatrix} \qquad \sigma_2 = \begin{pmatrix} 0 & -i \\ i & 0 \end{pmatrix} \qquad \sigma_3 = \begin{pmatrix} 1 & 0 \\ 0 & -1 \end{pmatrix}. \tag{2.28}$$

It should be noted that $(\gamma^0)^2 = I$ and $(\gamma^i)^2 = -I$. The 4 solutions to the Dirac equation for a free spin-1/2 particle shown in equation (2.24) correspond to spin up and spin down particles and antiparticles, as shown below.

Analogous to non-relativistic quantum mechanics, the plane wave solutions to the Dirac equation can be put forth as [1]

$$\psi(x^{\mu}) = u(p^{\mu})e^{-ix^{\mu}p_{\mu}}, \tag{2.29}$$

where $p^{\mu} = (E, \vec{p})$. On substituting equation (2.29) back in equation (2.23) the equation gets modified to its momentum space version.

$$(\gamma^{\mu}p_{\mu} - m)u = 0. \tag{2.30}$$

Further, using the definition of the γ matrices, and separating the space and the time components we get

$$\gamma^{\mu}p_{\mu} = \gamma^0 p_0 - \vec{\gamma} \cdot \vec{p} = \begin{pmatrix} E & -\vec{p} \cdot \vec{\sigma} \\ \vec{p} \cdot \vec{\sigma} & -E \end{pmatrix}, \tag{2.31}$$

which implies that

$$(\gamma^\mu p_\mu - m)u = \begin{pmatrix} (E-m)u_A & -\vec{p}\cdot\vec{\sigma}u_B \\ \vec{p}\cdot\vec{\sigma}u_A & -(E+m)u_B \end{pmatrix}, \tag{2.32}$$

where the 4 momentum spinor u is divided into two 2-component spinors u_A and u_B. The above further reduces to

$$\vec{p}\cdot\vec{\sigma}u_B = (E-m)u_A \tag{2.33}$$

$$\vec{p}\cdot\vec{\sigma}u_A = (E+m)u_B \tag{2.34}$$

Equations (2.33) and (2.34) yield the four independent solutions to the Dirac equation, corresponding to particles and antiparticles of spin up and down respectively. It is important at this stage to define a vector operator $\vec{\Sigma}$, which relates to the intrinsic spin

$$\vec{S} = \frac{\hbar}{2}\vec{\Sigma}, \tag{2.35}$$

so that

$$\vec{\Sigma}\cdot\hat{p} = \begin{pmatrix} \vec{\sigma} & 0 \\ 0 & \vec{\sigma} \end{pmatrix}\cdot\hat{p} \tag{2.36}$$

commutes with the free particle Dirac Hamiltonian. Since $\vec{\Sigma}\cdot\hat{p}$ also commutes with $\hat{p}$, $\{H, \vec{\Sigma}\cdot\hat{p}, \hat{p}\}$ form a complete set of mutually commuting operators and can be simultaneously diagonalized. Therefore the $\vec{\Sigma}\cdot\hat{p}$ operator, which tells us the projection of the spin along the direction of motion and has two eigenvalues ± 1, corresponds to a quantum number called helicity (h) that can be used to label the solutions to the Dirac equation [1, 13]

2.2.3 Symmetries of the weak interaction

Symmetry refers to an invariance of a system under a set of transformations. It plays an important role in the studies of fundamental particles and their interactions, as it manifests a link to the dynamics of the system. Furthermore, there exist a fundamental theorem called Noether's theorem [1], which states that for every symmetry there exist a corresponding conservation law. Broadly, in the study of physical systems there exist two kinds of symmetries.

- Discrete symmetries, such as parity, charge-conjugation etc.

- Continuous symmetries, such as rotations, space/time translations, etc.

The former lead to multiplicative conservation laws while the latter lead to additive conservation laws. In the former, the three important symmetries are parity, charge-conjugation and time-reversal. Parity (P) and time-reversal (T) transformations are referred to as space-time inversions as they change the space and time coordinates of the system under study, whereas the charge-conjugation (C) deals with the internal attributes of the system. The charge-conjugation operator transforms particles to antiparticles and vice-versa. One of the most important symmetries of the physical laws that arises from Lorentz invariance is called CPT symmetry, which refers to the simultaneous transformations under charge-conjugation, parity and time-reversal. This is known to be an exact symmetry for physical systems, whose violation is not permitted at the most fundamental level. In what follows below, I discuss the symmetry of parity (or mirror symmetry) which holds utmost importance in weak interaction phenomena.

2.2.4 Parity violation

In essence, a parity transformation refers to the rotation of a system through a polar angle of π, followed by inversion with respect to the intersecting axis. The parity operator is such that, for a given wave function

$$\hat{P}\psi(t, \vec{r}) \to \psi(t, -\vec{r}), \tag{2.37}$$

where the transformation in polar coordinates is $\hat{P}\psi(r, \theta, \phi) = \psi(r, \theta - \pi, \phi + \pi)$. This is pictorially shown below.
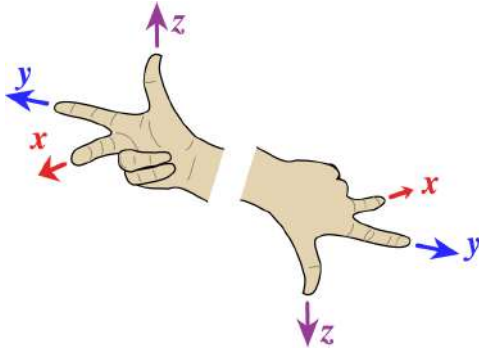
Figure 2.4: Representation of parity transformation for a hand.

It was not until the 1950s and later that a violation of the C, P and T symmetries were independently observed in nature. Initially the decay of two particles, the τ and the θ raised questions about parity symmetry. These particles seemed identical and had the same mass, charge, spin, etc, but their decay resulted into two different products,

$$
\begin{aligned}
\theta &\to \pi^+ \pi^0 \\
\tau &\to \pi^+ \pi^+ \pi^-.
\end{aligned}
\tag{2.38}
$$

Considering the multiplicative property of parity, since the intrinsic parity of a pion was measured to be $P = -1$, the final state for θ decay had an even ($P = +1$) parity, whereas for the τ it had an odd ($P = -1$) parity. This mystery was solved by Lee and Yang [14], who proposed that parity was violated in weak interactions and that the θ and the τ were just one particle, which was eventually identified as the kaon (K^+). This hypothesis was validated by a famous experiment performed by C. S. Wu and collaborators [15]. In the experiment, samples of ^{60}Co were spin polarized using an applied magnetic field near absolute zero (to minimize thermal fluctuations). On carefully observing the direction of emitted electrons from the β decay

$$
^{60}\text{Co} \to^{60} \text{Ni} + e^- + \bar{\nu}_e,
\tag{2.39}
$$

with respect to the polarization axis and obtaining alternating data sets after reversing the direction of the magnetic field, Wu and collaborators found the surprising result that the electrons were emitted preferentially

17

in the direction opposite to the polarization. If parity was indeed a good symmetry the angular distribution of electrons would have been equal in both directions relative to the polarization axis. So parity was indeed violated in β decays. Further experiments revealed that neutrinos emitted in a β decay are left-handed or they have negative helicity ($h = -1$) [16]. After
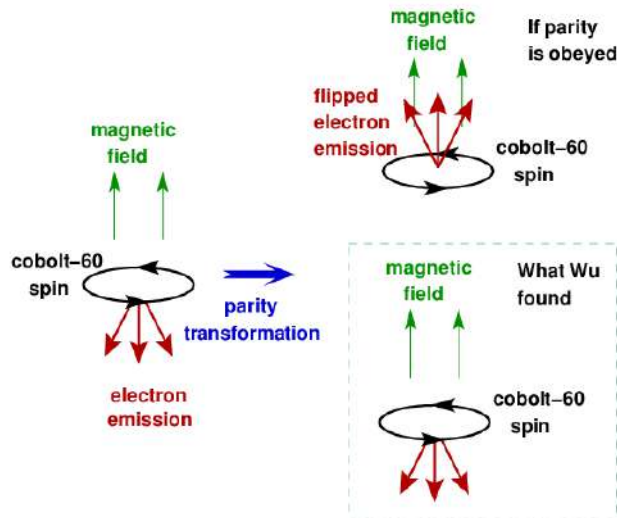
Figure 2.5: A schematic representation of the experiment of C. S. Wu and collaborators.

several decades of experimental searches, it is now firmly established that the neutrinos indeed are left handed, while anti-neutrinos are right handed (have helicity $+1$). This leads to the conclusion that parity is *maximally violated* in weak interactions.

2.2.5 Bilinear covariants of the Dirac spinors

In a relativistic description of the leptons following β decays, it is interesting to form products of the γ matrices and construct 16 linearly independent 4×4 matrices that transform differently under Lorentz boosts and space reflections. We define an adjoint spinor

$$\bar{\psi} \equiv \psi^\dagger \gamma^0 = (\psi_1^* \; \psi_2^* - \psi_3^* - \psi_4^*) \tag{2.40}$$

18

and introduce a new γ matrix

$$\gamma^5 \equiv i\gamma^0\gamma^1\gamma^2\gamma^3 = \begin{pmatrix} 0 & I \\ I & 0 \end{pmatrix} \tag{2.41}$$

Using the above definitions, one can write the hermitian conjugate of the Dirac equation as

$$i\partial_\mu\bar{\psi}\gamma^\mu + m\bar{\psi} = 0. \tag{2.42}$$

From equations (2.23) and (2.42), on multiplying the former by $\bar{\psi}$ from the left and the latter by ψ from the right and adding, we obtain the continuity equation

$$\partial_\mu(\bar{\psi}\gamma^\mu\psi) = 0, \tag{2.43}$$

where $j^\mu = \bar{\psi}\gamma^\mu\psi$ takes the form of a probability current. Based on the above the electromagnetic current density for a spin 1/2 charged particle can be defined as

$$j^\mu = -e\bar{\psi}\gamma^\mu\psi \tag{2.44}$$

Analogously, one can obtain the most general bilinear combinations for weak interaction currents shown in the table below, that transform differently under C, P and T.

Table 2.2: Summary of transformation properties for all possible bilinear currents

Transformation type	Bilinear current
Scalar	$\bar{\psi}\psi$
Pseudoscalar	$\bar{\psi}\gamma_5\psi$
Vector	$\bar{\psi}\gamma^\mu\psi$
Axial Vector	$\bar{\psi}\gamma^\mu\gamma_5\psi$
Tensor†	$\bar{\psi}\sigma^{\mu\nu}\psi$

$^\dagger\,\sigma^{\mu\nu} = \frac{i}{2}(\gamma^\mu\gamma^\nu - \gamma^\nu\gamma^\mu)$

2.2.6 The current-current interaction

Enrico Fermi [1] formulated one of the earliest theories of β decay using a Hamiltonian based on a current-current interaction, analogous to quantum electrodynamics. The electromagnetic interaction was successfully described in QED as a coupling of current density j_μ with a vector potential A_μ, so that the Hamiltonian is

$$H_{EM} = -ej_\mu A^\mu = -e\bar{\psi}\gamma_\mu \psi A^\mu. \tag{2.45}$$

Similarly, Fermi proposed the weak interaction Hamiltonian to be a current-current interaction of hadronic and leptonic currents

$$H_\beta = \frac{G_F}{\sqrt{2}} j^\mu j_\mu^\dagger, \tag{2.46}$$

where the weak current

$$j_\mu = j_\mu^h + j_\mu^l, \tag{2.47}$$

with h and l representing the hadronic and leptonic currents respectively. Explicitly, the interaction for a semi leptonic process such as nuclear β decay can be expressed as

$$H_\beta = \frac{G_F}{\sqrt{2}} (\bar{\psi}_p \hat{O} \psi_n)(\bar{\psi}_e \hat{O} \psi_\gamma) + \mathrm{h} \cdot \mathrm{c} \tag{2.48}$$

where $\mathrm{h} \cdot \mathrm{c}$ stands for hermitian conjugate and $\hat{O}$ is the operator responsible for the decay. Based on Lorentz invariance alone, these weak interaction currents can have the transformation properties listed in Table 2.2, where the operators transform similarly. Within the Standard Model, weak interactions are supposedly only of the $V - A$ (vector, minus axial-vector) type. As mentioned previously, this assumption is based purely on experiment, as there is no fundamental reason that forbids the presence of scalar, vector or pseudoscalar weak interaction currents. The observed maximal parity violation and measured helicities of the neutrinos and antineutrinos together with the lack of evidence for any other type of weak interaction indicate that $\hat{O}$ should be of the form

$$\hat{O} = (\gamma_\mu - \gamma_\mu \gamma^5). \tag{2.49}$$

20

In the above the required negative helicity states are projected out from the Hamiltonian. In its most general form, the $V - A$ Hamiltonian for nuclear β decays is written as

$$H_\beta = \frac{G_F}{\sqrt{2}} \underbrace{[\bar{\psi}_p \gamma_\mu (C_V - C_A \gamma_5) \psi_n]}_{\text{hadronic current}} \underbrace{[\bar{\psi}_e \gamma_\mu (C_V - C_A \gamma_5) \psi_{\bar{\nu}_e}]}_{\text{leptonic current}} + \text{h} \cdot \text{c}. \qquad (2.50)$$

where C_V and C_A are the strengths of the vector and axial vector couplings, relative to the universal Fermi coupling constant.

2.2.7 Description of β decays at quark level

A beta decay is essentially a transformation of one quark to another via the exchange of a W boson. For example, figure 2.6 shows a neutron β decay, which is the conversion of a down quark to an up quark via the exchange of a W^- boson [17]. Within the Standard Model, β decays are described such
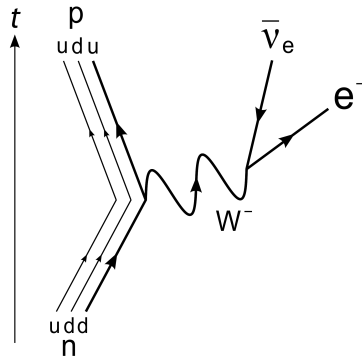
Figure 2.6: Feynman diagram of neutron decay at the quark level.

that the W bosons couple to only left-handed neutrinos (and right-handed antineutrinos), as mentioned previously. Thus, the quarks and leptons participate in weak interactions form doublets of left-handed fermionic states that comprise three generations,

$$\begin{pmatrix} \nu_e \\ e \end{pmatrix} \quad \begin{pmatrix} \nu_\mu \\ \mu \end{pmatrix} \quad \begin{pmatrix} \nu_\tau \\ \tau \end{pmatrix}$$

and

$$\begin{pmatrix} u \\ d \end{pmatrix} \quad \begin{pmatrix} c \\ s \end{pmatrix} \quad \begin{pmatrix} t \\ b \end{pmatrix}.$$

While in the case of leptons the coupling to the $W^\pm$ always takes place within a doublet, experiment shows that this is not the case for quarks. In fact, the coupling constants for the $u \leftrightarrow d$ or $c \leftrightarrow s$ transformations g_{ud} and g_{us} are found to be different than what one could expect for a *universal* weak interaction. Furthermore, decays such as $s \rightarrow u + W^+$ were measured experimentally.
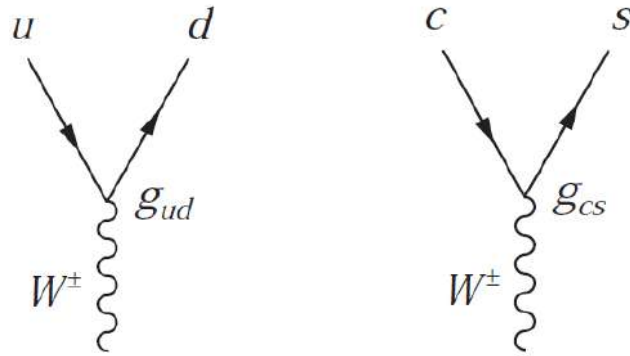
Figure 2.7: Feynman diagrams for two possible quark decays involving W bosons.

This prompted Cabibbo to suggest the phenomenon of quark mixing [12] which was further extended to three generations of quarks following the Glashow, Iliopolis and Maiani (GIM) mechanism [18] in the Cabibbo-Kobayashi-Maskawa matrix. In the present scheme, the charged weak current is known to couple to states in a rotated eigenbasis, so that the actual quark generations that participate in weak interactions are

$$\begin{pmatrix} u \\ d' \end{pmatrix} \quad \begin{pmatrix} c \\ s' \end{pmatrix} \quad \begin{pmatrix} t \\ b' \end{pmatrix},$$

where

$$\begin{pmatrix} d' \\ s' \\ b' \end{pmatrix} = \begin{pmatrix} V_{ud} & V_{us} & V_{ub} \\ V_{cd} & V_{cs} & V_{cb} \\ V_{td} & V_{ts} & V_{tb} \end{pmatrix} \begin{pmatrix} d \\ s \\ b \end{pmatrix}. \qquad (2.51)$$

The 3×3 matrix above is called the Cabibbo-Kobayashi-Maskawa (CKM) matrix. Within the SM, the CKM matrix is supposed to be unitary, so that

$$|V_{ud}|^2 + |V_{us}|^2 + |V_{ub}|^2 = 1. \tag{2.52}$$

Any deviations from unitary opens the room for beyond the standard model (BSM) physics. Of the three elements in the first row, V_{ud} has the largest value, which is experimentally determined from ft value measurements in nuclear β decays. In the non-relativistic limit, the V and A operators for a nuclear β decay (γ_μ and $\gamma_\mu\gamma_5$) reduce to the Fermi and Gamow-Teller operators $\vec{\tau}$ and $\vec{\sigma}\vec{\tau}$. In the *allowed approximation* for β decays, the leptons do not contribute to a change in the orbital angular momentum. This leads to a total momentum change of $\Delta J = 0$ or $\Delta J = 0, \pm 1$ between the parent and daughter states respectively. These selection rules characterize Fermi and Gamow-Teller decays.

For the special case of $0^+ \rightarrow 0^+$ β decays, called superallowed Fermi decays, since there is no change in total angular momentum, these transitions only make use of the vector weak coupling. The axial-vector coupling vanishes to the lowest order for this transitions. Feynman and Gell-Mann postulated that the vector coupling constant is conserved in weak interactions [19]. Thus, the measured ft values of $0^+ \rightarrow 0^+$ β decays should be independent of the nuclei in which they were measured. It is known that on applying small corrections to account for nuclear structure and radiative effects [20], the corrected ft values are indeed constant for several $0^+ \rightarrow 0^+$ β decays between isospin $T = 1$ states,

$$\mathcal{F}t = ft(1 + \delta_R)(1 - \delta_C) = \frac{K}{2G_F^2 V_{ud}^2 (1 + \Delta_R^V)}. \tag{2.53}$$

In the above K is a constant, δ_c is a nuclear structure dependent isospin violating correction and δ_R and Δ_R^V are radiative corrections. The vector coupling constant $G_V = G_F V_{ud} C_V$ obtained from the measured ft value is finally used to determine V_{ud}. It is apparent from equation (2.51) that the coupling for the hadronic part of the weak current for a nuclear β decay, which is essentially a $u \leftrightarrow d$ transformation, is reduced by a factor V_{ud}, so

that

$$H_\beta = \frac{G_F}{\sqrt{2}} V_{ud} [\bar{\psi}_p \gamma_\mu (C_V - C_A \gamma_5) \psi_n][\bar{\psi}_e \gamma_\mu (C_V - C_A \gamma_5) \psi_{\bar{\nu}_e}] + \text{h} \cdot \text{c}. \quad (2.54)$$

In its most general form, that allows for non $V - A$ interactions, the weak Hamiltonian for a nuclear β decay is written as

$$H_\beta = \frac{G_F}{\sqrt{2}} V_{ud} (\bar{\psi}_p \hat{O} \psi_n)[\bar{\psi}_e (C_i + C' \gamma_5) \psi_\nu] \quad (2.55)$$

where $i = S, V, T, A, P$ and the primed and unprimed coupling constants represents the strength of both parity conserving and parity violating components. Within the SM, the $V - A$ form of weak interaction is currently established so that $C_V = C'_V = 1$, $C_A = -C'_A$ and $C_i = C'_i = 0$ for $i \neq V, A$.

Chapter 3

The Special Case of ^{19}Ne β Decay

3.1 Angular Distributions, Correlations And Right-Handed Currents.

In several theoretical extensions to the SM, parity breakdown is assumed to be simply a low energy approximation, and the symmetry is restored at higher energies [21, 22]. These generalised left-right symmetric theories allow the existence of new right-handed gauge bosons. These right-handed bosons (W_2) with mass m_2 mix with the known left-handed bosons (W_1) with mass m_1 so that eigenstates that participate in the weak interaction are represented in these models by [22]

$$
\begin{aligned}
W_L &= \cos \zeta W_1 + \sin \zeta W_2 \\
W_R &= -\sin \zeta W_1 + \cos \zeta W_2,
\end{aligned}
\tag{3.1}
$$

where W_1 and W_2 are left and right-handed mass eigenstates and ζ is the left-right mixing angle. Jackson, Treiman and Wyld [23, 24], derived expressions for various observables in nuclear β decays that offer a means to extract the coupling constants of equation (2.55) experimentally. Thus, measurements of these observables allow for probes of BSM physics, including right-handed currents. In particular, the angular distribution and correlations of electrons

and neutrinos emitted from the decay is

$$\omega(\langle\vec{J}\rangle, \vec{\sigma}|E_e, \Omega_e, \Omega_\nu) \propto F(\pm Z, E_e) p_e E_e (E_f - E_e)^2 dE_e d\Omega_e d\Omega_\nu \times$$
$$\xi\left\{1 + \frac{\vec{p_e}\cdot\vec{p_\nu}}{E_e E_\nu}a + \frac{m}{E_e}b + \frac{\vec{J}}{J}\cdot\left[\frac{\vec{p_e}}{E_e}A + \frac{\vec{p_\nu}}{E_\nu}B + \frac{\vec{p_e}\times\vec{p_\nu}}{E_e E_\nu}D\right]\right\}, \qquad (3.2)$$

where $\langle\vec{J}\rangle$ is the nuclear polarization, $E, \vec{p}, \Omega$ are energy, momentum and angular coordinates of the leptons, m is the electron rest mass, E_f is the endpoint energy, $F(\pm Z, E_e)$ is the Fermi function and the accompanying correlation coefficients are listed below

- a is the $\beta - \nu$ correlation

- b is the Fierz interference term

- A is the β asymmetry

- B is the ν asymmetry

- D is a triple correlation.

Indeed, it was a measurement of the beta asymmetry (A_β) by Madame Wu et al. that established parity violation in weak interactions for the first time. In equation (3.2), ξ is directly related to the fundamental coupling constants so that for allowed β decays

$$\xi = |M_F|^2(|C_S|^2 + |C_V|^2 + |C'_S|^2 + |C'_V|^2) + |M_{GT}|^2(|C_T|^2 + |C_A|^2 + |C'_T|^2 + |C'_A|^2),$$
$$(3.3)$$

where $|M_F|$ and $|M_{GT}|$ are the Fermi and Gamow-Teller matrix elements. Within the SM, since $C_V = C'_V = 1$, $C_A = -C'_A$ and all other couplings are zero, ξ reduces to

$$\xi = 2\left[|M_F|^2 C_V^2 + |M_{GT}|^2 C_A^2\right]. \qquad (3.4)$$

As shown in figure 1.2 the β decay of ^{19}Ne proceeds predominantly to the ground state in ^{19}F. Such a β transition in which the parent and daughter are mirror isospin $T = 1/2$ doublets is called a superallowed mixed mirror transition. The word 'mixed' is used because both Fermi (vector) and

Gamow-Teller (axial-vector) matrix elements contribute to the transition. Given a certain electron capture probability (P_{EC}), the partial half-life for such a $1/2^+ \to 1/2^+$ β decay is

$$t = t_{1/2} \left[\frac{1 + P_{EC}}{BR} \right], \tag{3.5}$$

where BR is the $1/2^+ \to 1/2^+$ branching ratio. Using Fermi's golden rule and separating the vector and axial-vector phase space factors one can obtain the ft value of the decay analogous to equation (2.53) as [25]

$$f_{\rm v} t (1 + \delta_R)(1 - \delta_c) = \frac{K}{G_F^2 V_{ud}^2 |M_F|^2 C_V^2 (1 + \Delta_R^V)(1 + \frac{f_A}{f_V}\rho^2)}, \tag{3.6}$$

where we have defined the Gamow-Teller to Fermi mixing ratio as

$$\rho \simeq \frac{C_A M_{GT}}{C_V M_F}. \tag{3.7}$$

In terms of these new definitions one can reliably obtain Standard Model predictions for correlation coefficients in mixed mirror transitions, assuming purely $V - A$ weak interactions. For example, in the limit of zero momentum transfer we can obtain the β asymmetry [26]

$$A_\beta(0) = \frac{\rho^2 - 2\rho\sqrt{J(J+1)}}{(1+\rho^2)(J+1)}. \tag{3.8}$$

More generic expressions to obtain SM predictions for correlation coefficients that includes higher-order corrections (beyond the allowed approximation) are shown in Ref. [26]. In order to place meaningful bounds on right-handed currents using nuclear β decay, it is important to measure the ft value of the decay (to obtain ρ). This quantity will be used to obtain the SM prediction which can be compared to the measured β asymmetry. Any discrepancy between the calculated and measured values would signal new physics. As mentioned previously, the measured β asymmetry for ^{19}Ne β decay is known to have high sensitivity for right-handed currents [8]. This is not unexpected as it is a small value $A_\beta = -0.0391(14)$ [11]. A precise measurement of the ft value of the decay is further required to place stringent bounds on

new physics (such as right-handed currents, etc.). For this, one requires a precise measurement of the Q_{EC} value of the decay, the $1/2^+ \to 1/2^+$ branching ratio, the electron capture fraction and the half-life of ^{19}Ne. Although all the other observables have been measured recently [27, 28, 29, 30, 31], the $1/2^+ \to 1/2^+$ branch is not on a similarly secure footing. For completeness, in this thesis we report a new measurement of the $1/2^+ \to 1/2^+$ branch in ^{19}Ne β decay by detecting gamma-rays from the dexcitation of the 110 keV $1/2^-$ and the 1554 keV $3/2^+$ states in ^{19}F (see figure 1.2), at $E_\gamma = 110$ keV and $E_\gamma = 1356$ keV respectively. Unlike the previous measurements of Refs. [32, 33], our measurement uses a point source from a radioactive ion beam implanted onto a mylar-backed Aluminium tape. The previous measurements used a ^{19}F(p,n) reaction on gas targets. Efficiency determinations for such measurements are known to be challenging due to the diffuseness of the source distribution. It is anticipated that our measurement will not only aid in placing useful bounds on right-handed currents, it will also be part of useful data for future probes of tensor and scalar currents using ^{19}Ne β decay [31].

Chapter 4

Experimental Details

The ^{19}Ne β decay data described in this thesis was obtained using a ^{19}Ne radioactive beam and the 8π spectrometer at the ISAC facility, TRIUMF, Vancouver, Canada. In the following sections I briefly describe the facility, the equipment, and the techniques used for this particular experiment.

4.1 TRIUMF Facility

The Tri-University Meson Facility (TRIUMF) is the Canadian national laboratory for particle and nuclear physics founded by three Universities in Canada, Simon Fraser University, University of British Columbia (UBC) and University of Victoria. The facility is located on UBC campus. TRIUMF possesses one of the world's largest cyclotrons, shown in figure 4.1 that has the ability to accelerate proton beams up to an energy of 500 MeV with a maximum intensity up to $\sim$100 μA [4]. The characteristic advantage of the TRIUMF cyclotron over others is that it accelerates H$^-$ ions instead of ordinary protons. On passing the accelerated ions through thin stripper foils located at various positions, it becomes possible to produce two proton beams at each foil location, which bend in opposite directions to an applied magnetic field. This allows the cyclotron to accelerate proton beams to different experimental stations simultaneously.
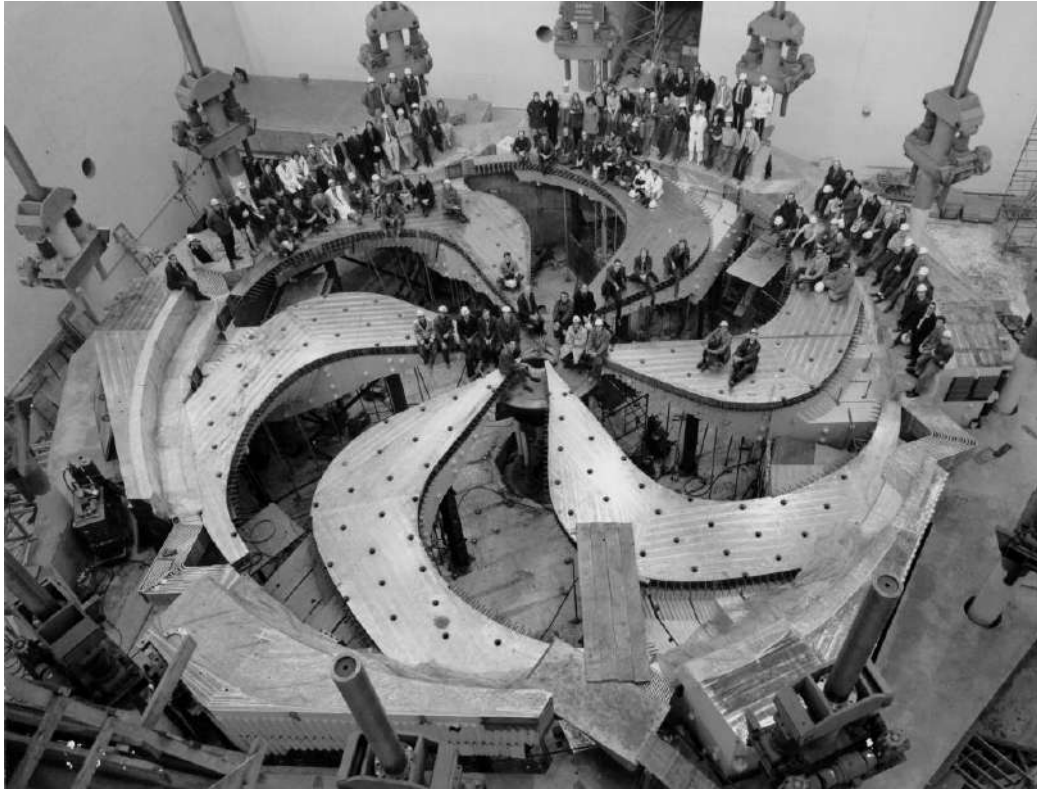
Figure 4.1: A photograph of the cycloton magnet sectors and staff at TRI-UMF (January 1972) [4].

4.2 ISAC At TRIUMF

The Isotope Separator and ACcelerator (ISAC) facility shown in figure 4.2 is located down the dedicated 100 μA beam line from the cyclotron [34]. This facility is dedicated for radioactive ion beam (RIB) experiments. For RIB production, a 500 MeV high intensity proton beam from the cyclotron is bombarded on a stationary target leading to the production of various radioactive isotopes via spallation reactions. These isotopes are then extracted from the target and ionized using either of the ionization sources: Electron Cyclotron-Resonant (ECR) source, TRIUMF-ISAC Resonant Laser Ionization Source (TRILIS) or Forced Electron Beam-Induced Arc Discharge (FEBIAD) [35].

The ^{19}Ne radioactive ions ($t_{1/2} \approx 17$ s) were produced for this experiment by bombarding a heated SiC target with 500 MeV protons. Radioactive
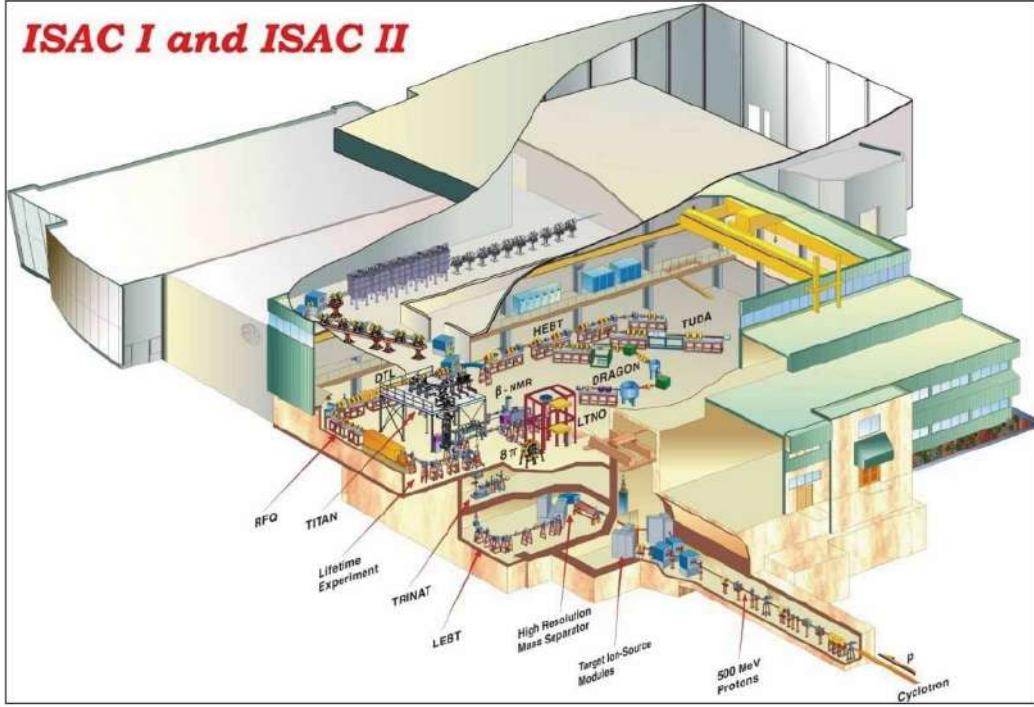
Figure 4.2: A diagram of the ISAC facility at TRIUMF.

neon atoms produced from the target were ionized using a FEBIAD (plasma) ion-source and mass selected using a high resolution mass separator, which seperated the ion trajectories based on their mass-to-charge ratio,

$$r = \frac{1}{B}\sqrt{\frac{2m\Delta V}{q}}, \tag{4.1}$$

where r is the radius of the ion orbit for a fixed m/q, B is the applied magnetic field, m is the mass of the ion, q is the ionic charge and ΔV is the applied potential difference, which is a maximum of 60 keV at the ISAC-I facility. For this experiment a beam of 37 keV ^{19}Ne ions with an intensity of $\sim 10^5$ ions s^{-1} was finally delivered to the 8π γ-ray spectrometer, which is described below.

31

4.3 The 8π Spectrometer

The 8π spectrometer used for decay spectroscopy at TRIUMF (following β decay) is comprised of 20 Compton suppressed γ-ray detectors, 20 plastic scintillator detectors (SCEPTAR) and a moving tape collector (MTC) system. The tape system is used to collect the radioactive ions and move any long-lived contaminant radioactivity away from the detector system. In the following subsections, I will describe these briefly.

4.3.1 The 8π γ-array

The 8π spectrometer in TRIUMF is an array of 20 spherically symmetric, Compton-suppressed High Purity Germanium Detectors (HPGe) shown in figure 4.3. It covers 13% of the 4π solid angle, with each detector placed in the position of a hexagon. The 20 detectors share one center forming the shape of a truncated icosahedron, the shape of a soccer ball, with two openings reserved for beam lines. The full array has an absolute detection efficiency of 1% at γ-ray energy of 1.3 MeV. As can be seen in figure 4.3,

(a) One hemisphere of the 8π spectrometer [4].
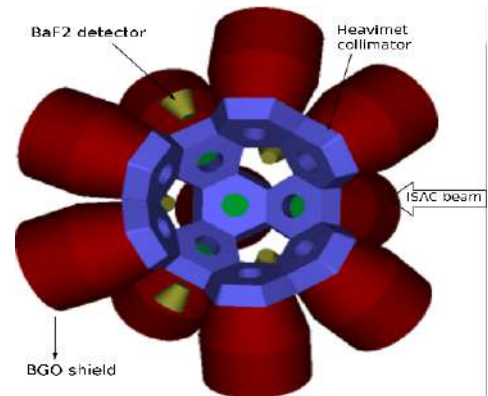
(b) A model of the 8π array used for Monte Carlo simulations described later. Various parts are labelled.

Figure 4.3

in addition to the BGO (Bismuth Germanate) Compton suppression shields,

heavy metal (Hevimet) collimators are placed on the front of the HPGe detectors, in order to avoid γ-rays from the source directly hitting the BGO shields.

4.3.2 SCEPTAR

The Scintillating Electron Positron Tagging Array (SCEPTAR), is a set of auxiliary detectors that accompanies the 8π HPGe array and covers $\sim 80\%$ of the total solid angle. It comprises of 20 plastic scintillators that are 1.6 mm thick, and positioned in the form of two rings of five trapezoidal shapes, two rings of rectangular shapes as shown in figure 4.4 and 4.5. The SCEPTAR array is housed inside the 8π spectrometer, in a one-to-one correspondence with HPGe detectors to collect $\beta - \gamma$ coincident data. The coincidences are collected in a narrow time window of a few μs, so that contributions from room background are greatly reduced [36].
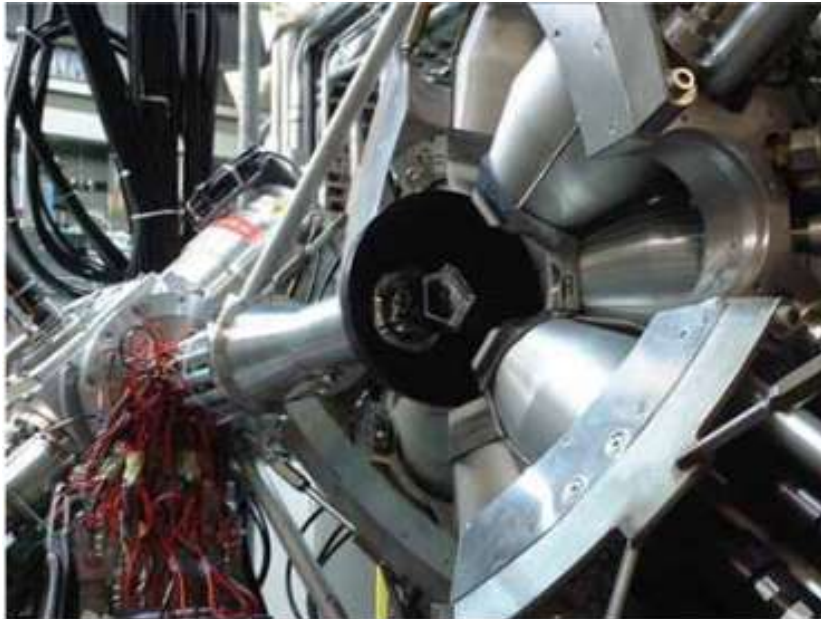
Figure 4.4: A picture of the downstream half of SCEPTAR detectors.

4.3.3 The moving tape collector (MTC) system

The MTC at the 8π spectrometer, is an approximately 120 m long tape that is roughly 13 mm wide and 50 μm thick [37]. The tape is made of either FeO coated mylar or thick Al with mylar backing. It is kept in vacuum, passing right through the center (front) of the downstream half of the SCEPTAR array (see figure 4.5). The continuous loop is kept at tension in front of the
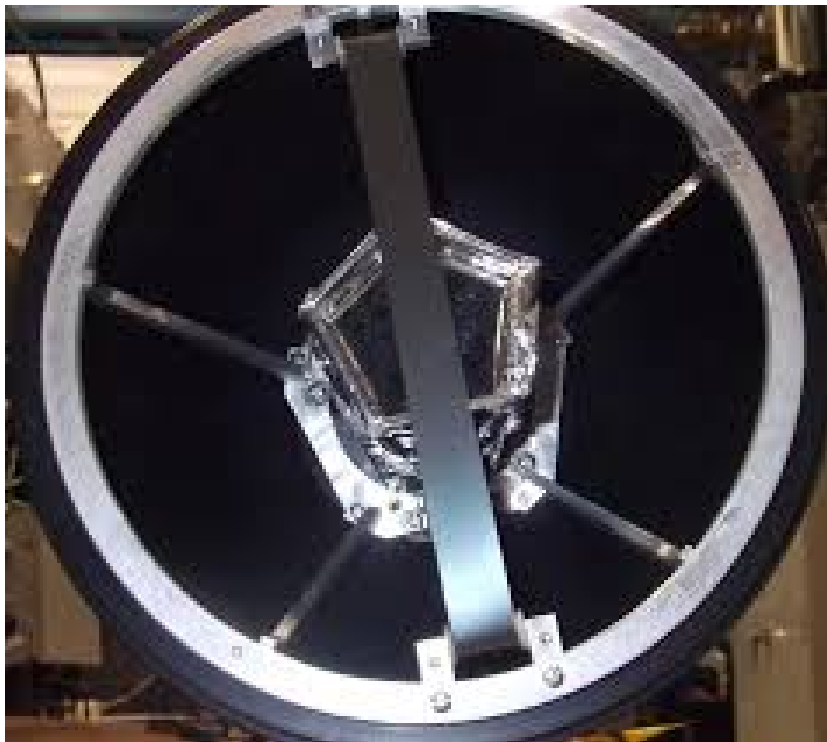
Figure 4.5: A photograph of the collection tape and the downstream half of SCEPTAR.

detectors and left loose inside a shielded lead box shown in figure 4.6. The tape box is situated at the back of the spectrometer, where the tape is moved into after a predetermined 'counting time' so as to isolate from the detectors any long-lived activity from contaminants in the beam. A motor is used to keep the tape in motion, to and from the box at certain intervals during the experiment. These time intervals are part of the 'tape cycles' used to collect the data.

4.4 The ^{19}Ne β Decay Experiment At TRIUMF

Figure 4.6: A photograph of the 8π array and the tape box for the MTC.

The experiment to determine the ft value of ^{19}Ne β decay consisted of two parts. In the first part data were collected using short implant times and long counting times for a precision half-life measurement. The cycle times were adjusted to take background data for 2 seconds, implant for 1 second and count for 300 seconds ($\sim$ 20 half-lives). This cycle is represented by 2-1-300-1, with the final 1 second reserved for tape movement to the box, before the next beam pulse comes in. The half-life measurement has already been published [27]. For the branching ratio measurement the tape cycle was changed to 4-25-1-1. The reason for the use of such different tape cycles for the two measurements will be apparent in the following chapters.

4.4.1 Data acquisition

Since the 8π array consists of 20 germanium detectors and allows for several other auxiliary detectors such as SCEPTAR and an array of BaF_2/LaBr and silicon detectors (not used for this experiment), there exists a certain complexity for the data acquisition system (DAQ), as different detector systems will have varying count rates. For this purpose, data streams from different detectors were read separately using analog nuclear instrumentation module (NIM) electronics [37]. For the γ-ray energy signals and their time stamps, two identical signals from each HPGe pre-amplifier were amplified in a Ortec 572 spectroscopy amplifier and then sent to Ortec AD114, 14-bit analog-to-digital converters (ADCs) for digitization. The timing signals were amplified by fast timing-filter amplifiers and discriminated with Ortec 583b constant fraction discriminators (CFDs). The timing signals were digitized using LeCroy 3377, 16-channel multi-hit time-to-digital converters (TDCs). These TDCs were also used to process timing signals from the BGO Compton suppression shields as well as pulse pileup signals from the spectroscopy amplifiers. Event-by-event time stamps are provided by a LeCroy 2367 universal logic module (ULM) and a precision Stanford Research Systems 10 MHz $\pm$ 0.1 Hz oscillator.

For the β particles, for each scintillator the signal was split into two. One PMT output was sent to Phillips Scientific 776 amplifier, and then to a LeCroy 4300 fast encoding read-out amplifier (FERA) and QDC (charge to digital converter). The second signal was sent to the Ortec 935 CFD and then is fed to a 32-channel SIS3801 virtual machine environment (VME) multi-channel scalar (MCS) module. The CFD signals are also sent to 16-channel multi-hit LeCroy 3372 TDCs for β timing.

For this particular experiment the master trigger for the 8π DAQ was set to take scaled down β singles, $\beta - \gamma$ coincidences or scaled down γ ray singles data, with a scale-down factor of 255.

Chapter 5

Data Analysis, Results and Conclusions

5.1 Energy and Efficiency Calibrations

Before I proceed to the description of the analysis of the ^{19}Ne β decay data, I will first describe the procedure used to obtain the γ-ray detection efficiencies, which is most important for branching ratio measurements. For this experiment, the efficiency and energy calibration of the detectors were performed using ^{152}Eu, ^{60}Co and ^{133}Ba sources that were placed at the center of the tape where the ^{19}Ne beam was implanted. The calibration procedure is described below.

5.1.1 Data preselection

The 8π γ-ray spectrometer is equipped with BGO (Bismuth Germanate) Compton-suppression shields that are used to reject Compton scattered events, enhancing the peak-to-background ratio. Although the BGO suppression for the HPGe detectors and the requirement of $\beta - \gamma$ coincidences were already set in hardware using the DAQ electronics, the acquired data from the 8π array (as well as SCEPTAR) were first preselected using software gates to reject random unwanted events that were not true coincidences. For example, in the calibration spectra described later, gates were applied on the prompt HPGe and BGO TDC times to ensure proper data preselection. These gates

37

for a single detector are shown in the figures below. As mentioned in the figure caption, the gap in figure 5.3 shows γ-ray events vetoed due to BGO suppression. Software gates shown in figure 5.2 were applied nonetheless for a more stringent requirement of the coincidences.
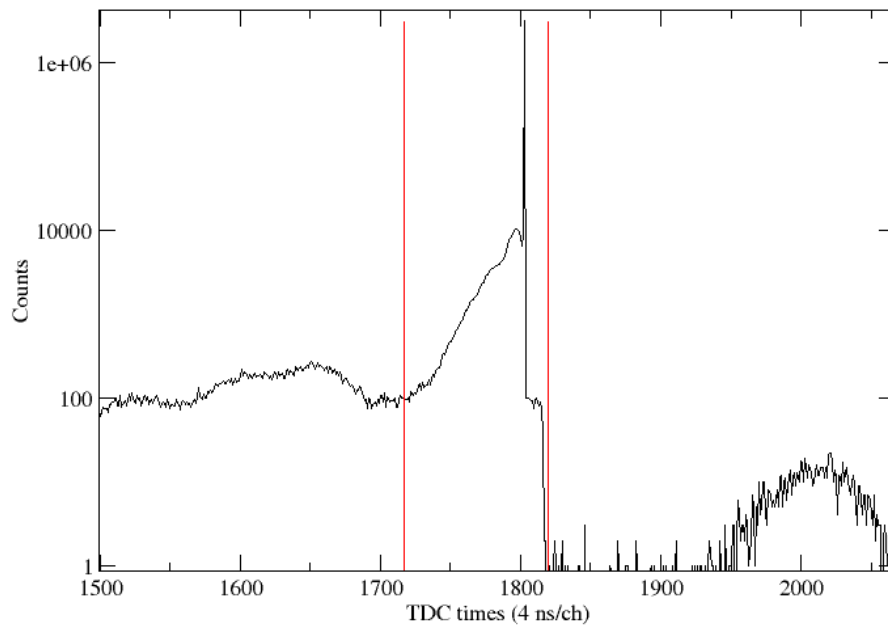

Figure 5.1: HPGe TDC spectrum for a single detector shown with the applied software time gate.
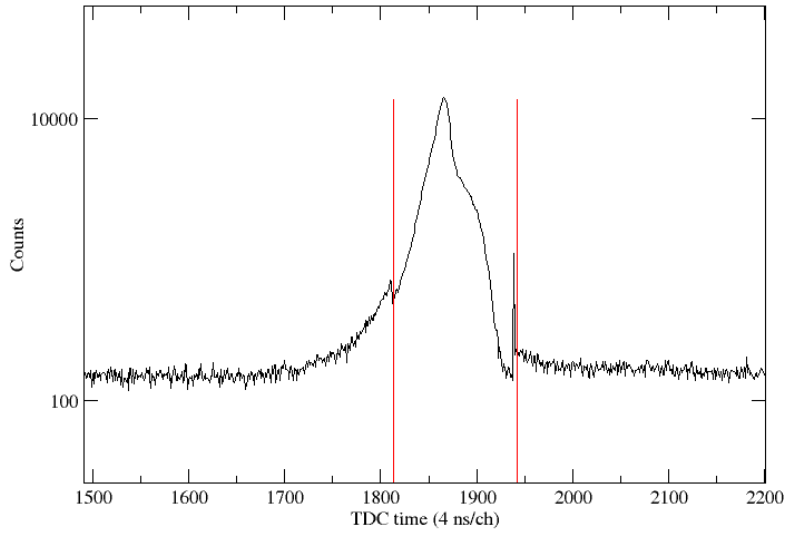
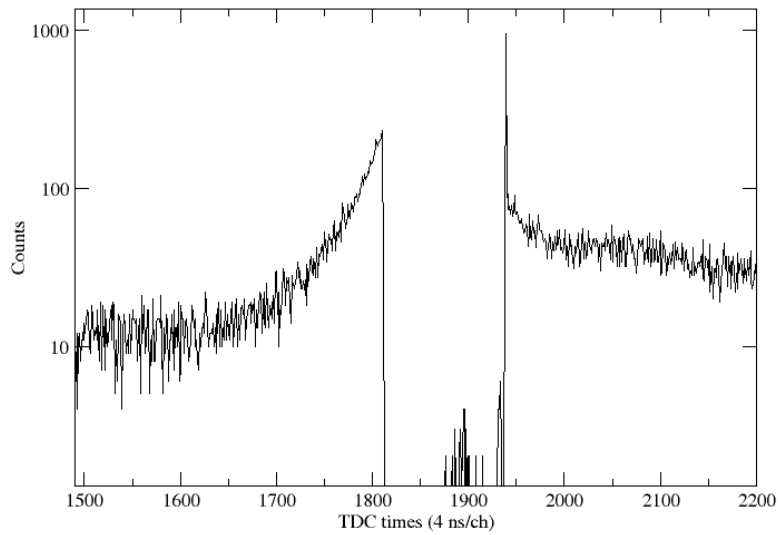Figure 5.2: BGO TDC spectrum for a single detector with the applied software time gate.

Figure 5.3: BGO TDC spectrum for a single detector showing the vetoed events due to hardware suppression.

39

5.1.2   Gain Shift Corrections

At the beginning of the experiment, the gain of each pulse shaping Ortec 572 spectroscopy amplifier is set to a constant factor. The role of this amplifier is to shape and amplify the pre-amplifier signal before sending it to AD114 ADCs. Such analog amplifiers are known to be sensitive to ambient temperature, leading to small changes in their gains over time. This results in a distortion of γ-ray peak shapes and in extreme cases leads to shifts in the peak centroids. Since the data analysis involves summing of γ-ray spectra from 20 HPGe detectors over a significant time duration, the spectra from each detector had the potential to be affected by a gain drift in its corresponding amplifier. This required 'gain drift corrections' for the 20 individual calibration spectra.

After data preselection, the time-stamped data from each HPGe detector were sorted so that the centroids of three selected peaks from each spectrum were registered for the data in each run which were divided into several 'sub-runs' with adequate statistics in each peak. The centroids were then corrected so that the centroids from each subsequent 'sub-run' were fitted with respect to the first 'sub-run' using a linear regression routine

$$x'_i = a_i + b_i x_i \tag{5.1}$$

to obtain the gains (and offsets) for data in each of these sub-runs as a function of time. Ideally, in the absence of gain drifts, all the gains (b_i) and offsets (a_i) for each subsequent sub-run would be 1 and 0 with respect to the first sub-run. Unfortunately this was not the case for our data, indicating that there were significant drifts. Once the gains and offsets of each sub-run was obtained, the data were resorted, and the correction coefficients for each sub-run were used to 'gain correct' the data to match the first sub-run using the equation

$$Ch_i = \{[Ch_i + (rand - 0.5)]b_i\} + a_i. \tag{5.2}$$
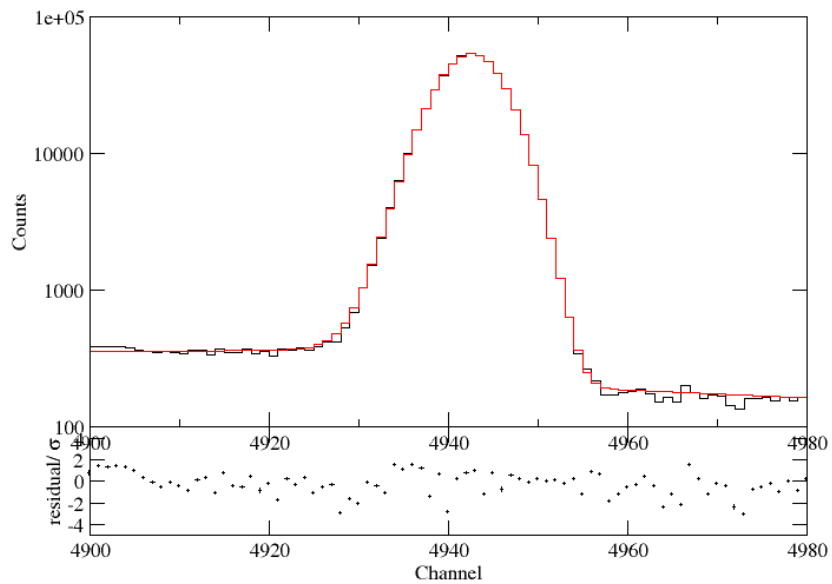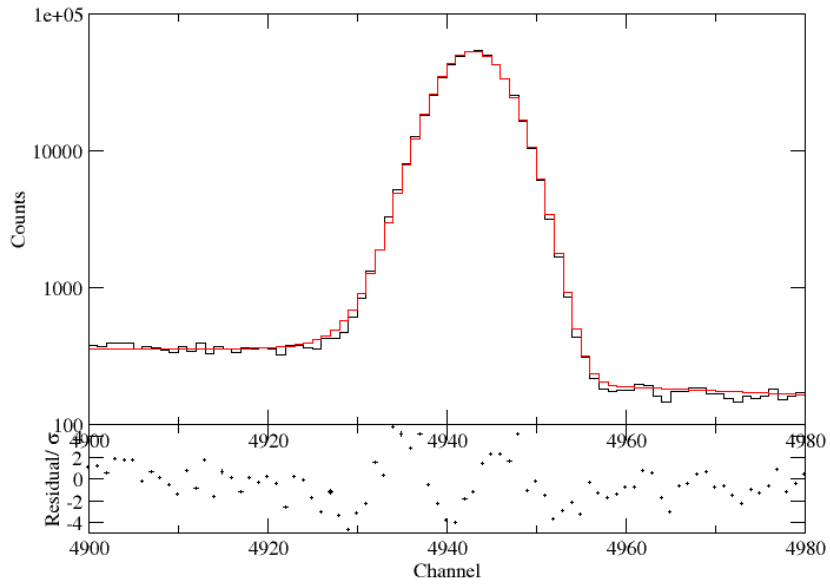
for i sub-runs, where $rand$ is a random number between 0 and 1.

Figure 5.4: Sample fit to an uncalibrated 1173 keV peak from ^{60}Co before and after gain drift corrections. The residuals in the bottom plot do not show as much oscillatory behaviour as in the top plot indicating that the corrections were indeed successful, leading to better fits to the data.

Figure 5.4, shows a sample spectrum with the 1173 keV peak from ^{60}Co. On fitting the peak using a standard function that is used for γ-ray analysis (the convolution of a Gaussian with a low energy exponential tail and a smoothed step function), we observe a marked improvement in the fit on applying the gain drift corrections. This allowed us to add the spectra from the 20 detectors with greater confidence.

5.1.3 Energy Calibration

An ADC converts the amplified and shaped detector signals into digital data. It determines the pulse height and according to its magnitude specified by amplifier, histograms the peak information corresponding to a channel number, which is proportional to the γ-ray energy. Energy calibration basically refers to the conversion of channel numbers (peak centroids) to energy units for each detector. For an array such as the 8π, an accurate energy calibration of each of the 20 Germanium detectors is important so that peaks in the spectra can be correctly identified and the spectra from the 20 detectors can be summed accurately. For the energy calibration of our data, photo peaks from the calibration sources were first fit to obtain the peak centroids. These peak centroids were then converted to energies for each detector using the linear relation

$$E_\gamma = a_0\mu + a_1, \tag{5.3}$$

where the μ's are centroids obtained from fits to the gain corrected, uncalibrated spectra. Sample energy-calibrated spectra from the three calibration sources used in this experiment are shown in the figures below.
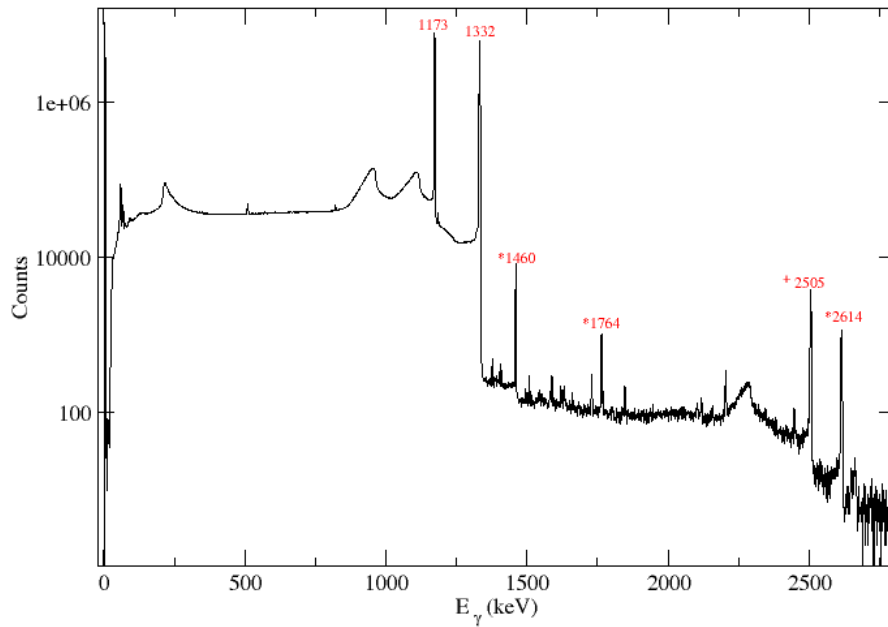
Figure 5.5: Calibrated spectrum from the ^{60}Co source, with the prominent peaks labelled.
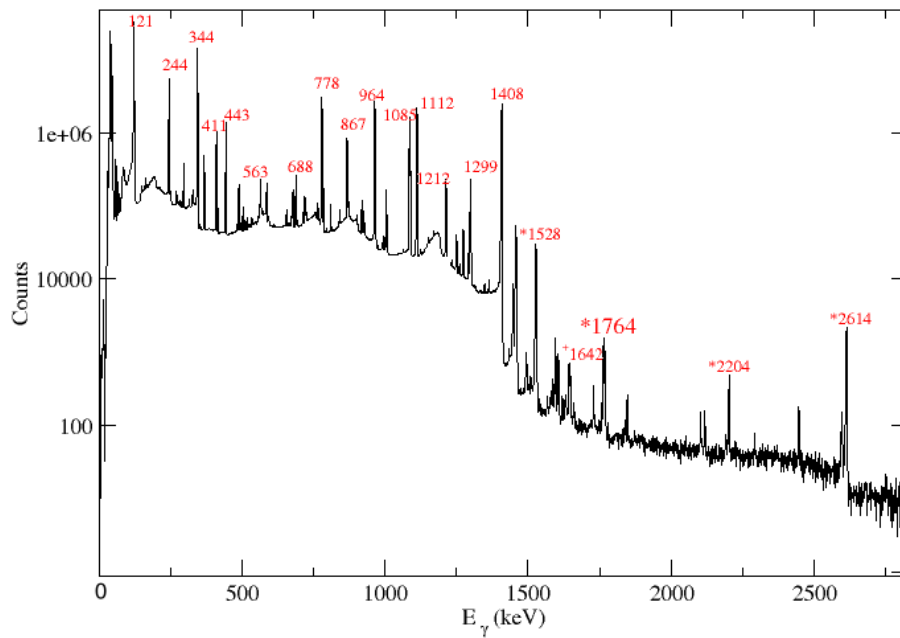
Figure 5.7: Calibrated spectrum from the ^{152}Eu source, with the prominent peaks labelled.

43
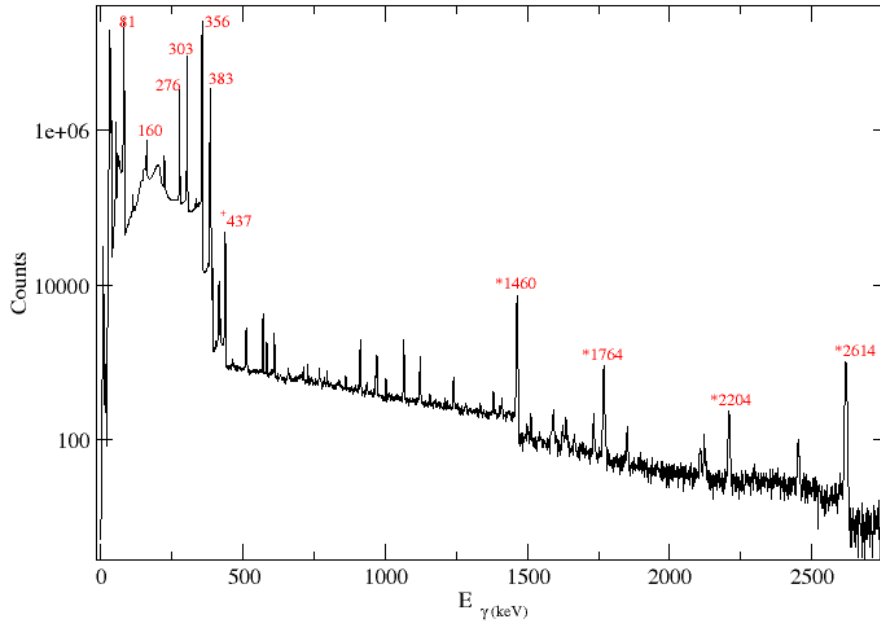
Figure 5.6: Calibrated spectrum from the ^{133}Ba source, with the prominent peaks labelled.

Figure 5.5, 5.6 and 5.7 show the γ-ray peaks in the calibration spectra that we identified from our analysis. In these figures, the starred ($*$) peaks indicate the peaks from room background, while those marked with a + sign indicate the peaks arising from coincidence summing, which is described in section 5.2.2.

5.2 Absolute Efficiency Calibration

As mentioned previously, a very important step for a precise determination of branching ratios via γ-ray spectroscopy is an absolute efficiency calibration of the detector system. The photo peak efficiency of the 8π array (or any γ-ray detector) is defined as the ratio of the absolute number of γ rays detected by the detector to the total number of photons emitted by the source. The γ-ray energies used for energy calibration, together with their intensities obtained from NNDC [38] were also used for the efficiency calibration of our data. This information is listed in Table 5.1.

44

Source	Energy keV	Intensity %	Source	Energy keV	Intensity %
^{152}Eu	121.7817 (3)	28.53 (16)	^{152}Eu	1112.076 (3)	13.67 (8)
^{152}Eu	244.6974 (8)	7.55 (4)	^{152}Eu	1212.948 (11)	1.415 (8)
^{152}Eu	295.9387 (17)	0.44 (4)	^{152}Eu	1299.142 (8)	1.633 (11)
^{152}Eu	344.2785 (12)	26.59 (20)	^{152}Eu	1408.006 (3)	20.87 (9)
^{152}Eu	367.7891 (20)	0.859 (6)	^{60}Co	1173.228 (3)	99.85 (3)
^{152}Eu	411.1165 (12)	2.237 (13)	^{60}Co	1332.492 (8)	99.9826 (6)
^{152}Eu	443.9606 (16)	2.827 (14)	^{133}Ba	80.9979 (11)	32.9 (5)
^{152}Eu	488.6792 (20)	0.414 (3)	^{133}Ba	160.612 (16)	0.63 (5)
^{152}Eu	563.986 (5)	0.494 (5)	^{133}Ba	223.2368 (13)	0.45 (3)
^{152}Eu	586.2648 (26)	0.455 (4)	^{133}Ba	276.3989 (12)	7.16 (5)
^{152}Eu	678.623 (5)	0.473 (4)	^{133}Ba	302.8508 (5)	18.3 (13)
^{152}Eu	688.670 (5)	0.856 (6)	^{133}Ba	356.0129 (7)	62.0
^{152}Eu	867.380 (3)	4.23 (3)	^{133}Ba	383.8485 (12)	8.94 (6)

Table 5.1: Information used for energy and efficiency calibration of the detectors.

Before the final absolute γ-ray detection efficiency curve for the 8π array is determined, it is important that certain corrections be performed to the data. I describe these below.

5.2.1 Pulse pile-up correction

Pulse pile-up in γ-ray spectroscopy occurs where pulses from two or more consecutive γ rays from separate decays are detected and processed by the ADC while it is integrating the charge collected by the first event. This leads to false events due to pulse 'pile-up'. For a precise detector efficiency calibration, it is important that these pile-up effects are corrected, particularly if the event rate is high. In order to correct for these, a pile-up signal was generated from the 'busy' output of the 572 spectroscopy amplifiers and recorded as a pile-up TDC time. While sorting the data, wide gates were placed on the pile-up TDC times so that almost all the 'busy' events were considered to be piled-up events. Then, a pile-up probability was calculated

for each run (for all 20 detectors) [39]

$$\rho = \frac{PU}{PU + NPU},$$ (5.4)

where PU stands for the number of the γ-ray events with good TDC times that have pile-up triggers and NP is the number of γ-ray events with good TDC times with no corresponding pile-up triggers in the run. The summed areas for each energy calibrated photo peak was corrected for pile up effects using the formula

$$A'_{det}(\text{all}) = \frac{1}{1-\rho} \sum_{i=1}^{20} A_{det}(i),$$ (5.5)

where 'all' stands for the 20 HPGe detectors in the 8π array.

5.2.2   Summing Corrections

Coincidence summing occurs when a radioactive source has at least two energy levels that γ decay to lower states in the form of cascades, as shown in figure 5.8. If the solid angle subtended by the detectors is significant, then there is a high probability that the two γ rays show up as a summed photo peak.
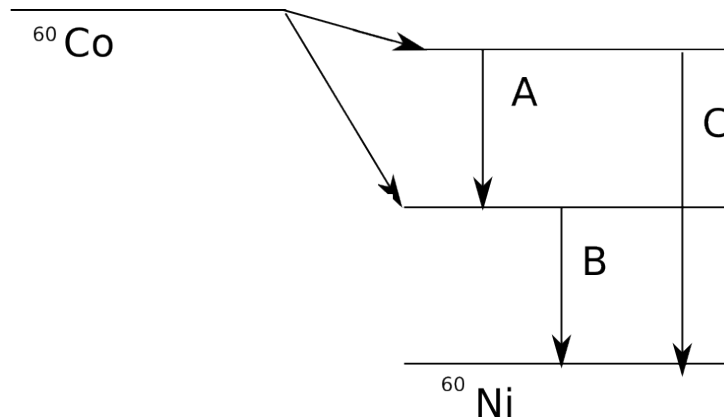

Figure 5.8: A γ-ray cascade highlighting the effect of coincidence summing.

As shown in figure 5.8, if three transitions A, B and C are allowed in a hypothetical nucleus, summing effects (A+B) can lead to extra counts in

the photo peak corresponding to C. Such a γ-ray cascade will not only yield an increased efficiency for the γ-ray labelled C, it will also reduce the measured efficiency for γ rays labelled A and B. Since all our calibration sources produce γ rays mainly by cascades, it was important for us to investigate summing effects in our efficiency calibrations. It is apparent from figures 5.5, 5.6 and 5.7 that there is a clear evidence of summed peaks in the 8π calibration spectra. In order to determine summing corrections to the photo peak areas, we performed Monte Carlo simulations using a Fortran based radiation transport code called PENELOPE (Penetration and ENErgy LOss of Positrons and Electrons) [40], which allows for the simulation of electrons, photons and positrons and their interactions and transport in arbitrary materials that could have complex geometries [40].

To perform the simulations, first the entire geometry of the 8π was built within PENELOPE, with specifications of the detectors, BGO shields, heavimet collimators, SCEPTAR detector, Al tape etc. The geometry used for the simulations is shown below.
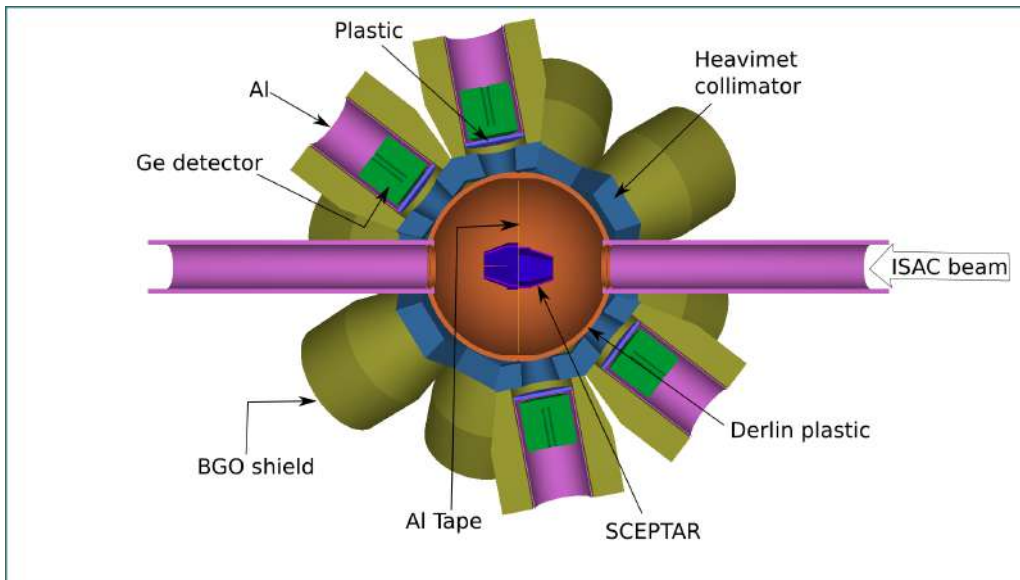

Figure 5.9: Cross section of geometry of the 8π array with SCEPTAR and tape system designed for the simulations.
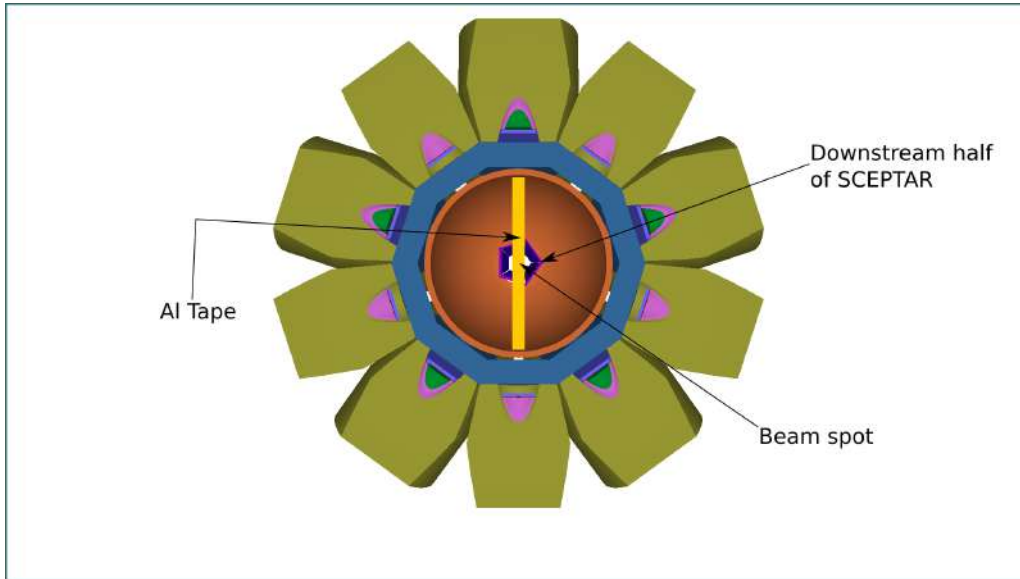
Figure 5.10: Another cross section of the 8π detector system used in the simulations.

Figure 5.10 shows the geometry of the array along the beam axis, clearly indicating the implantation region on the tape.

In order to obtain the summing corrections, two sets of simulations were performed. In the first set, γ rays corresponding to ones from the calibration sources were emitted isotropically from the implantation region of the tape (where the sources were placed) and the events registered by the HPGe detectors were histogrammed and the total γ-ray detection efficiency for the array was determined ($\epsilon_{singles}$). In the second set, the PENELOPE code was modified so that the complete decay scheme was input into the code as a subroutine (with all the β branches and γ-ray intensities obtained from NNDC), so that the relevant cascades could be generated. Once this was established to be working correctly, the efficiency for each HPGe detector was determined and summed similarly as before ($\epsilon_{cascades}$). The validity of our simulations was verified by taking the ratios of areas under the summed peaks (shown in figures 5.5, 5.6 and 5.7) to the 'unsummed' peaks from the simulation, which was compared to experiment. The simulations are in excellent agreement

with the data, as shown in Table 5.2 below. Summing corrections for peak areas of each γ-ray for the total array were finally determined using simple expression

$$k = \frac{\epsilon_{\text{singles}}}{\epsilon_{\text{cascades}}}. \tag{5.6}$$

Table 5.2: The summing ratios obtained for the simulated as well as experimental data for the identified summed peaks.

$\mathbf{E}_\gamma$(summed) keV	$\mathbf{E}_\gamma$(unsummed) keV	$\mathbf{N}_\gamma$(summed)/$\mathbf{N}_\gamma$(unsummed) in %	
		experiment	simulation
1123	344	0.084 (4)	0.08 (3)
	778	0.37 (2)	0.3 (1)
2505	1173	0.0849 (6)	0.10 (2)
	1332	0.0949 (7)	0.11 (2)

5.2.3 Absolute Efficiency

Once the pile-up and summing-corrected peak areas were obtained, these values were used to determine the absolute photo peak detection efficiencies. The ^{60}Co source of activity 29.75(59) kBq was first used to obtain the absolute efficiencies at energies $E_\gamma = 1173$ keV and $E_\gamma = 1332$ keV. This is because the activity of the ^{60}Co source was most well known. The efficiency of each γ-ray was determined using the expression

$$\epsilon_\gamma = \frac{N(i)}{A_\gamma(i)}, \tag{5.7}$$

where $N(i)$ is the corrected peak area and $A_\gamma(i)$ is the activity of the source for each γ-ray,

$$A_\gamma(i) = AI_\gamma(i)T_L, \tag{5.8}$$

with A being the source activity, $I_\gamma(i)$ being the intensity of the ith γ-ray and T_L being the live time of the runs used to collect the data. Once the absolute

efficiencies of these two γ rays were determined, the ^{152}Eu and ^{133}Ba γ yields were used to determine the relative efficiencies from the expression

$$\epsilon_\gamma^{rel}(i) = \frac{N(i)}{I_\gamma(i)}. \tag{5.9}$$

Next, the relative efficiencies for the peaks from the ^{152}Eu source were fitted to the polynomial

$$\ln \epsilon_\gamma^{rel}(i) = \sum_{j=0}^{4} a_j \left[\ln E_\gamma(i)\right]^j, \tag{5.10}$$

to obtain 'relative' efficiencies at 1173 keV and 1332 keV. These efficiencies were then normalized to the absolute efficiencies of the ^{60}Co peaks. The same procedure was used to normalize the ^{133}Ba γ ray spectrum to the ^{152}Eu γ-ray spectrum in the region of overlapping energies. This procedure gave us absolute efficiencies in the energy range from 81 keV $\leq$ E$_\gamma$ $\leq$ 1408 keV. The extracted efficiencies are listed in Table 5.3. On plotting these values and fitting an efficiency curve through the data using a polynomial similar to equation (5.10), we obtain the efficiency of the 8π at $E_\gamma = 110$ keV to be $\epsilon_\gamma = 6.8\,(2)$ % and at $E_\gamma = 1357$ keV to be $\epsilon_\gamma = 1.066(17)\%$. The efficiency curve is plotted in figure 5.11 below, with the efficiencies of the two γ-rays from ^{19}Ne at 110 keV and 1357 keV highlighted.

Table 5.3: Absolute efficiencies for the 8π from all sources, for energies ranging from 81 keV to 1408 keV.

| Source	Energy keV	Summing Correction %	Efficiency %
^{133}Ba	80.9979 (11)	0.948 (4)	6.02 (9)
^{152}Eu	121.7817 (3)	1.406 (2)	9.47 (6)
^{133}Ba	160.612 (16)	0.970 (2)	6.16 (6)
^{133}Ba	223.2368 (13)	1.042 (2)	5.16 (4)
^{152}Eu	244.6974 (8)	1.177 (2)	5.52 (3)
^{133}Ba	276.3989 (12)	1.023 (2)	4.29 (3)
^{152}Eu	295.9387 (17)	1.018 (2)	3.8 (3)
^{133}Ba	302.8508 (5)	0.987 (2)	3.83 (3)
^{133}Ba	356.0129 (7)	0.986 (2)	3.19 (2)
^{152}Eu	367.7891 (20)	1.137 (2)	3.83 (2)
^{133}Ba	383.8485 (12)	0.962 (2)	3.05 (3)
^{152}Eu	443.9606 (16)	1.030 (2)	3.04 (2)
^{152}Eu	488.6792 (20)	1.262 (3)	3.09 (2)
^{152}Eu	688.670 (5)	1.009 (3)	2.90 (2)
^{152}Eu	1112.076 (3)	1.148 (6)	1.43 (1)
^{60}Co	1173.228 (3)	0.913 (4)	1.05 (2))
^{152}Eu	1212.948 (11)	0.968 (5)	1.112 (8))
^{60}Co	1332.492 (8)	0.990 (5)	1.09 (2))
^{152}Eu	1408.006 (3)	0.992 (3)	1.111 (8))
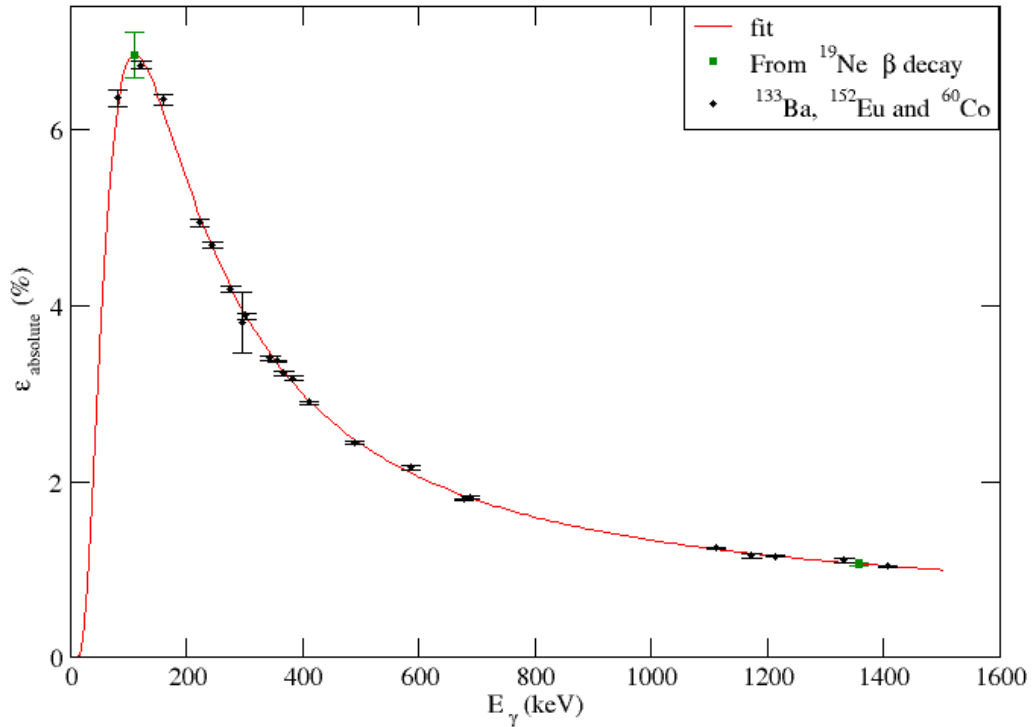
Figure 5.11: Absolute efficiency curve of the whole 8π array, covering a range of energies from 81 keV to 1408 keV. The efficiencies at 110 keV and 1357 keV are determined from the fit.

5.3 ^{19}Ne Data Analysis

The radioactive ^{19}Ne atoms implanted into the 8π tape decay to states in the ^{19}F daughter nucleus, consequently emitting positrons particles as well as γ rays. Therefore the analysis of its data requires the analysis of data streams from both SCEPTAR and the 8π detectors. For the analysis of these data, similarly as before, the data were preselected using prompt TDC gates on the γ-ray, BGO and SCEPTAR time spectra (for all 40 β and γ-ray detectors). Further software gates were applied on the SCEPTAR energy spectra to ignore low energy events and other events that arise from the charge-integration of the QDC's for the detectors that did not trigger. These latter events show up in a pedestal peak as shown in figure 5.12. Examples of SCEPTAR energy and time gates that are shown in figures 5.12 and 5.13.
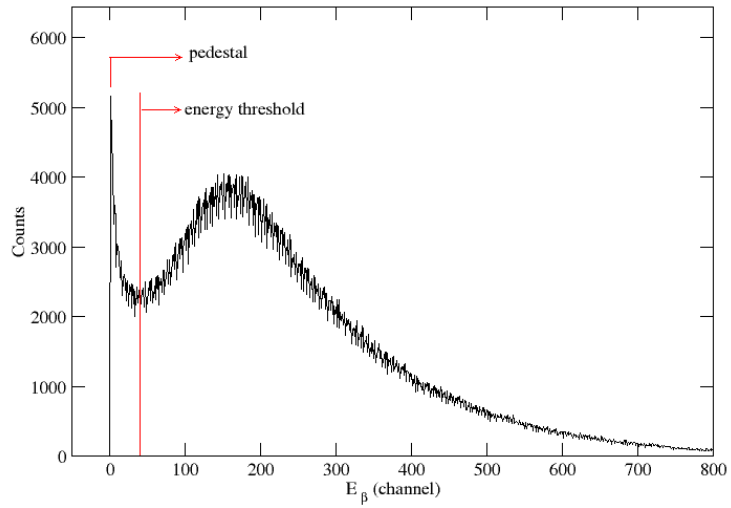
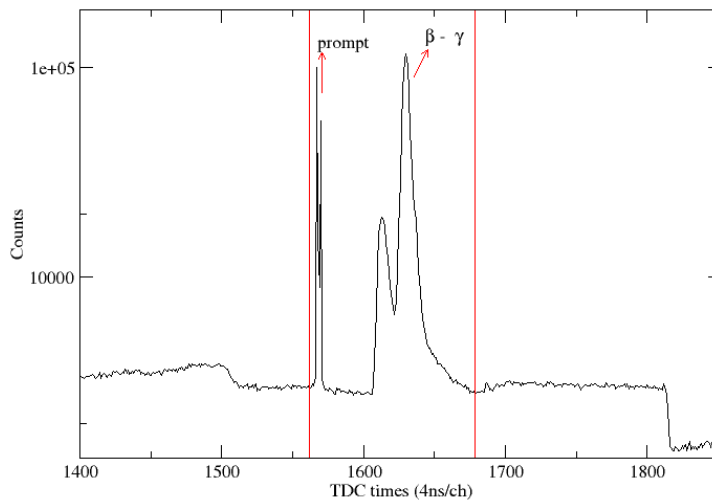Figure 5.12: QDC spectrum for a single SCEPTAR detector with the high-lighted low energy threshold.

Figure 5.13: TDC spectrum for a single SCEPTAR detector with the applied accepted time gates.

53

As mentioned before the master trigger for the 8π DAQ was set to take data with scaled-down γ singles or scaled-down β singles or $\gamma - \gamma$ coincidences or $\beta - \gamma$ coincidences, with a scale-down factor of 255. Thus to place stringent gates to obtain $\beta - \gamma$ coincidence data information, further software gates were applied to minimize the background from the singles data and from random coincidences. In order to place these gates, the 10 MHz clock was used to obtain the time differences between the master triggers of both SCEPTAR and HPGe arrays using the Universal Logic Module (ULM). The $\beta - \gamma$ coincidence gate, shown in figure 5.14 was $\approx 20~\mu$s wide and was used to obtain the coincidence spectra.
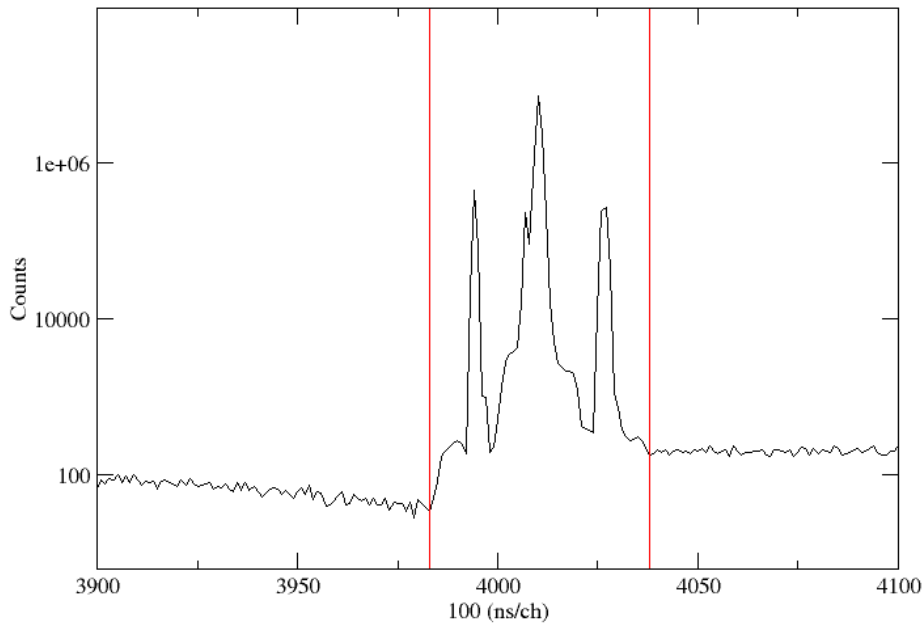

Figure 5.14: The ULM time difference spectrum with the allocated time gates for the $\beta - \gamma$ coincidences. The side peaks represents true events where ULM occasionally dropped bits.

5.3.1 Cycle selection

As discussed in Section 4.4, the ^{19}Ne β decay data were collected using tape cycles. In each tape cycle, background data were taken for 4 seconds, following which the beam was collected on tape for 25 seconds and 1 second was used for tape movement. There were times during the cycles when beam was lost due to instabilities with the cyclotron and the ion source. Tape cycles during which such beam related losses were observed were discarded from the analysis. The ULM was used to generate histograms of the total number of β counts registered by SCEPTAR per cycle. Figure 5.15 shows one such example. For a constant data rate this ULM spectrum ought to have a flat distribution. However, as shown in an example in figure 5.15, several cycles in many runs had much lower statistics indicating beam related losses. These cycles were rejected from the data analysis by imposing a threshold below which the cycles were rejected using the sort code.
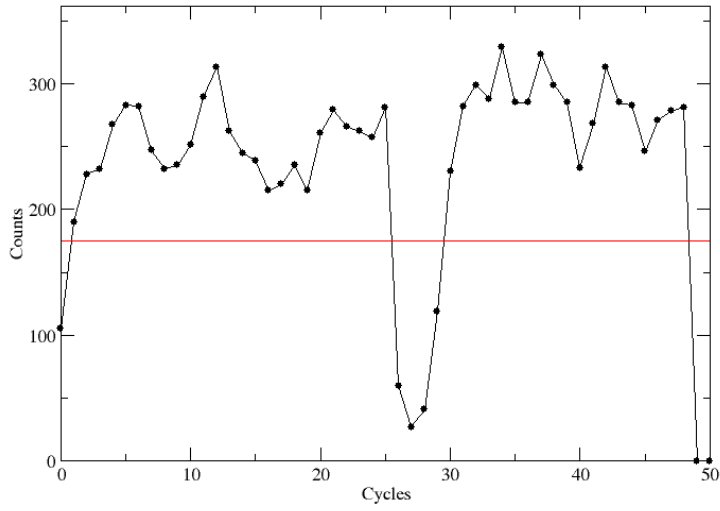
(a)
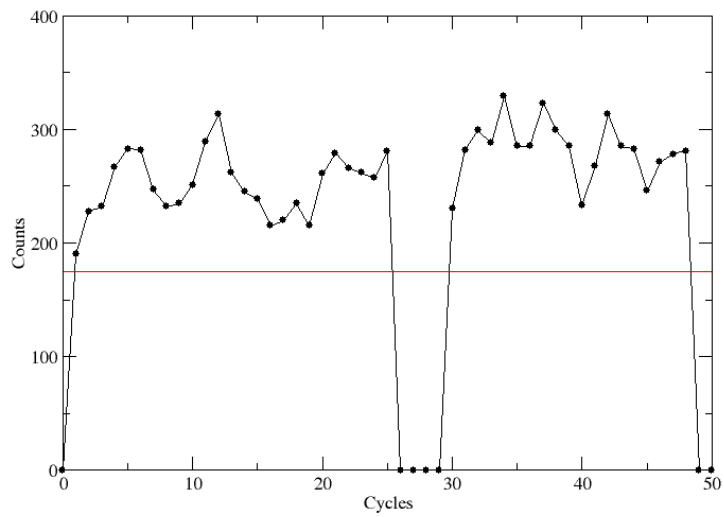
(b)

Figure 5.15: An example run with histogrammed cycle number versus number of β counts detected by SCEPTAR. The bad cycles from cycle number 26 to 29 were rejected if the counts fell below the highlighted thresholds.

5.4 Extraction of the $1/2^+ \rightarrow 1/2^+$ Branch

5.4.1 β counting and dead time corrections.

For the determination of absolute β decay branches one needs a measure of the total number of ^{19}Ne atoms that decayed in our analysis window. This is the same as the total number of β events detected by the SCEPTAR array in the same analysis window. However, before obtaining the integrated β counts, it is important that the data be corrected for data acquisition dead time. This is because the β particles in each cycle continuously trigger the data acquisition system. Since the system processes every event over a finite amount of time, during this time it can not accept the other events. This results in the loss of true β counts. The non-responsive time of the DAQ described above is called the dead time. This effect is rate dependent and ought to be corrected in order to determine a precise branching ratio. The dead-time-corrected integrated β counts for cycled data can be obtained using the expression [39]

$$N'(i) = \frac{N(i)}{1 - N(i)(\frac{\tau}{t_b N_c})}, \tag{5.11}$$

where $N(i)$ is the measured value, τ is the effective dead time per event, t_b is the bin size and N_c is the total number of cycles. The effective dead time for the combination of β singles as well as $\beta - \gamma$ coincidences is obtained using

$$\tau = \frac{(N_\beta \times t_d^\beta) + (N_{\beta\gamma} \times t_d^\gamma)}{(255 \times N_\beta) + N_{\beta\gamma}}. \tag{5.12}$$

where N_β is the number of β singles events, $N_{\beta\gamma}$ is the number of coincidence events and t_d^β and t_d^γ are the average dead times of SCEPTAR and 8π respectively. The latter were determined on an event-by-event basis with the 10 MHz clock and scalars, which were histogrammed and averaged. An example of the histogrammed dead times for SCEPTAR is shown in figure 5.16 below.
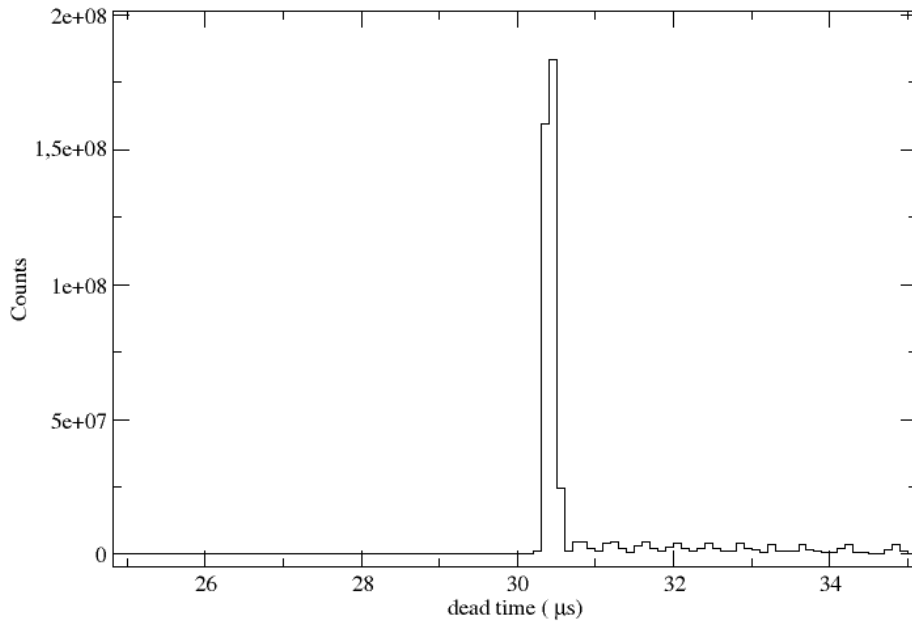
Figure 5.16: Histogram of event-by-event dead times for the SCEPTAR array.

Figure 5.17 is a histogram of the β counts for all cycles over the cycle time of 31 s, before and after dead time corrections. The corrections were performed using the average values $t_d^\beta = 30.35$ μs, $t_d^\gamma = 30.30$ μs, which yielded an effective dead time per event of $\tau = 0.12$ μs for all events over a total of 1382 accepted cycles.
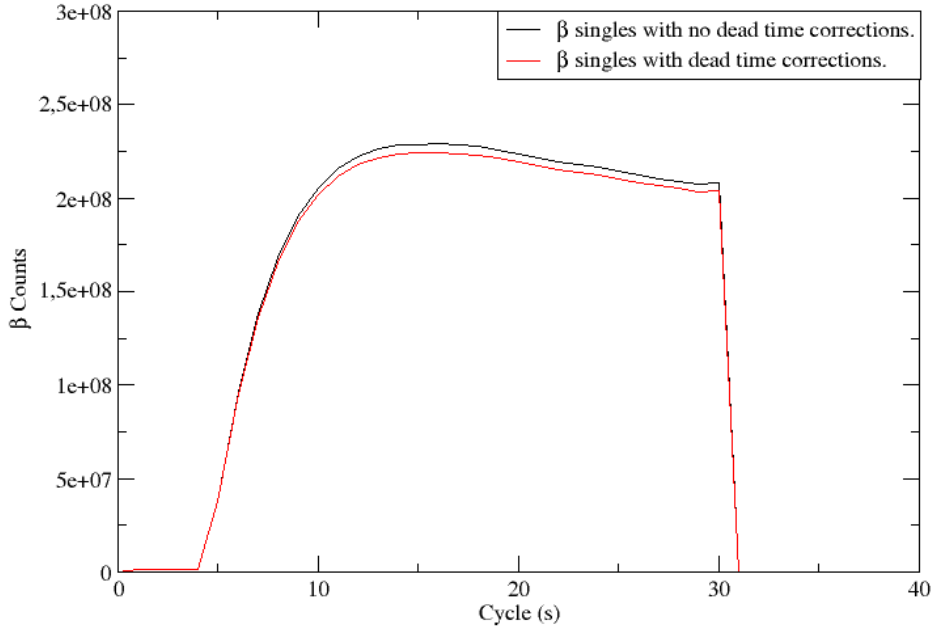
Figure 5.17: The β singles spectra for both dead time corrected and uncorrected events for all accepted cycles.

5.4.2 Determination of β^+ branching ratios

The observed γ rays feeding the ground state of ^{19}F are populated by weak β branches of ^{19}Ne decay. These intensities were used to obtain the $1/2^+ \rightarrow 1/2^+$ branch from ^{19}Ne to ^{19}F. As shown in the ^{19}Ne decay scheme in figure 5.18 below, γ-rays, with energies of $E_\gamma = 110$ keV, $E_\gamma = 1357$ keV and $E_\gamma = 197$ keV are supposed to be observed following the β decay, based on allowed selection rules. Our $\beta - \gamma$ coincidence spectrum in figure 5.19 and 5.20 clearly shows the 110 keV and 1356 keV γ rays, but the 197 keV γ is missing due to the large Compton shoulder (background) in that energy region. However, since the 1357 keV transition feeds the 197 keV level 100% of the time, this does not affect our determination of the branches.
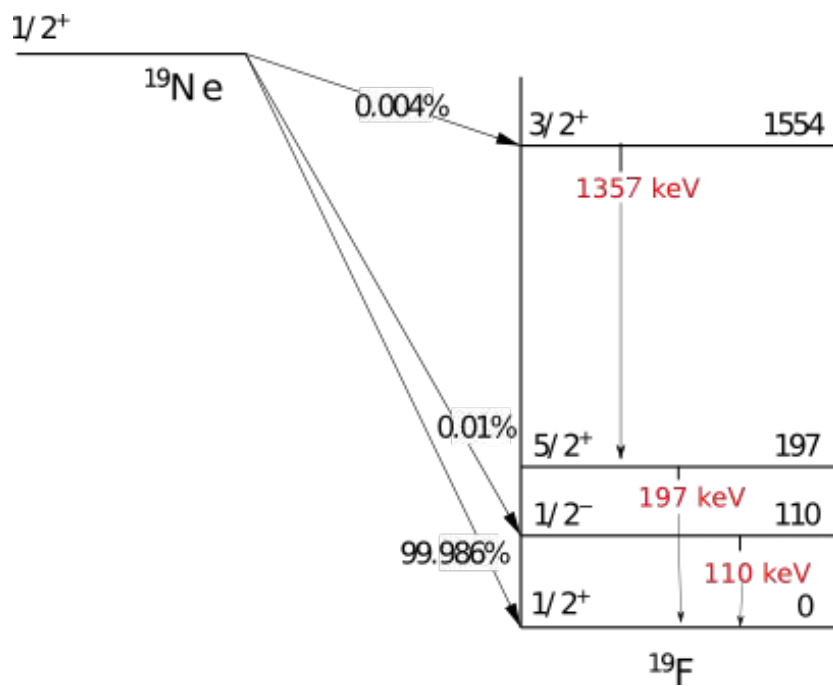
Figure 5.18: A ^{19}Ne decay scheme clearly indicating the γ rays emitted following the β decay.

Figure 5.19 shows a comparison of the spectra obtained with and without the coincidence gate of figure 5.14. While there is a significant change in the background level, many of the background peaks are still visible in the coincidence spectrum, most probably due to the high rate of positrons causing random coincidences.

Figure 5.19: Spectrum of γ rays following ^{19}Ne β decay observed before and after applying the $\beta - \gamma$ coincidence gate.

The most prominent γ-ray peaks from ^{19}Ne β decay are labelled in figure 5.19. Figure 5.20 shows zoomed in regions of the $\beta - \gamma$ coincidence spectrum highlighting the two peaks of interest at E_γ=110 keV and E_γ=1357 keV.

Figure 5.20: Delayed γ rays from ^{19}Ne β decay in the coincidence spectrum .

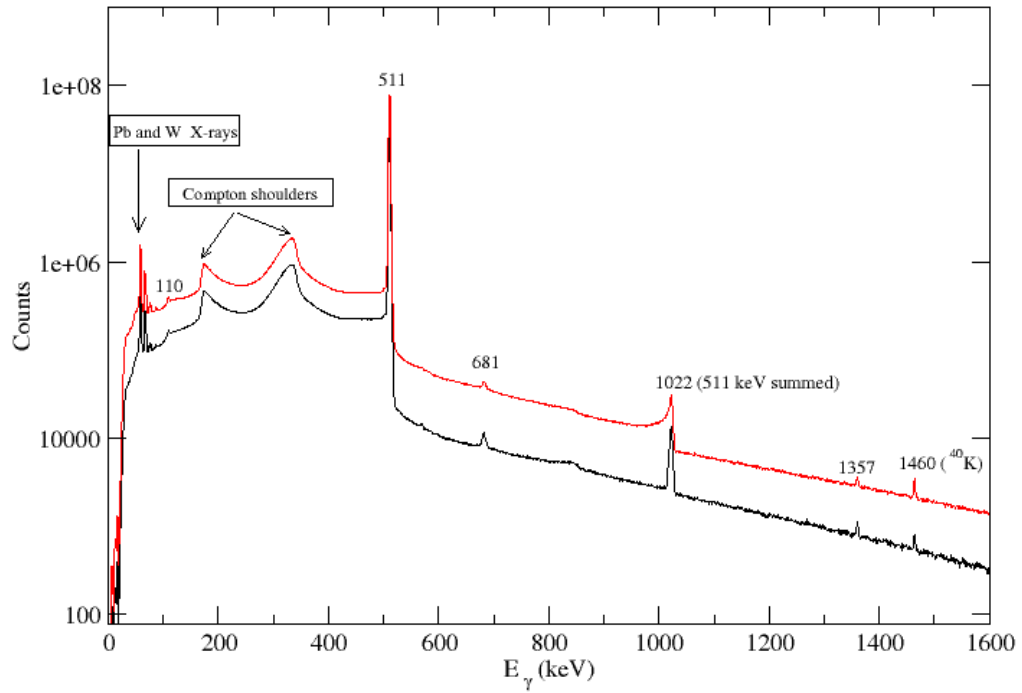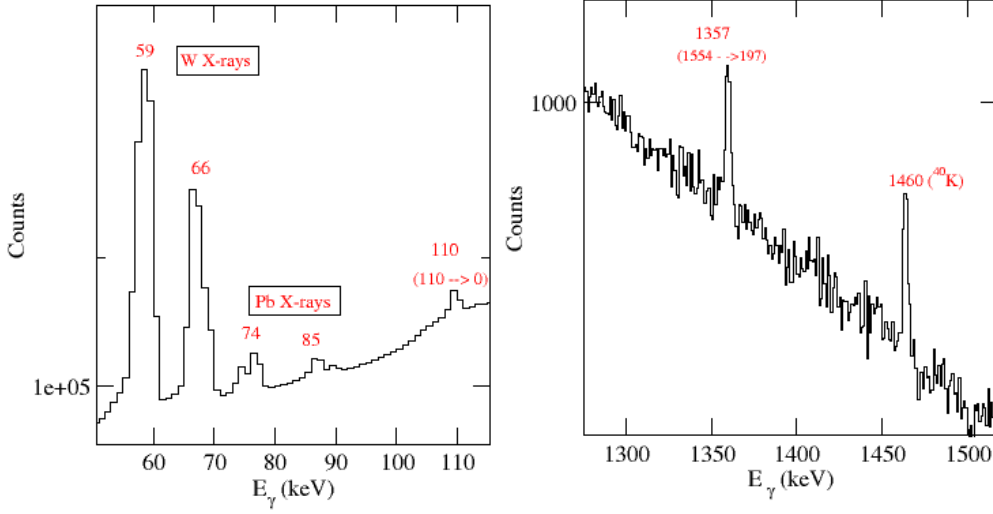The number of counts for these γ-rays is determined by fitting the data using the Levenberg-Marquardt algorithm [41]. The γ-ray lineshape function that was used for the fits is described in Ref. [42], Appendix A. It is essentially a convolution of a Gaussian with two exponential tails, one of which serves as a smoothed step function. The peaks were assumed to be sitting on a linear background, which was kept as a free parameter in the fits. All correlations were taken into considerations in the evaluation of the final uncertainty in the extracted peak areas.

The β-decay branching ratios to the $1/2^-$ state in ^{19}F at 110 keV and the $3/2^+$ state in ^{19}F at 1554 keV were obtained using the formula

$$BR(i) = \frac{N_{\beta\gamma}(i)}{\epsilon_\gamma(i) \times N_\beta}. \qquad (5.13)$$

This formula assumes the β detection efficiency to be independent of the β energy and accounts for the proper dead time and pile-up corrections for $N_{\beta\gamma}$ and N_β. The branch to the $5/2^+$ state in ^{19}F is negligible as it is a $\Delta J = 4$ β transition, which is third-forbidden and therefore highly suppressed.

Once these branching ratios were determined, the branch to the ground state can be obtained using the formula

$$BR(1/2^+ \rightarrow 1/2^+) = 1 - BR(110 \text{ keV}) - BR(1357 \text{ keV}). \qquad (5.14)$$

The summary of the results is given in Table 5.4 below.

Table 5.4: Results from this work

Branch	ϵ_γ %	BR(this work) %	BR(previous work)[25] %
$1/2^+ \rightarrow 3/2^+$	6.8 (2)	0.0111 (5)	0.012 (2)
$1/2^+ \rightarrow 1/2^-$	1.07 (2)	0.0023 (2)	0.0022 (2)
$1/2^+ \rightarrow 1/2^+$	-	99.9866 (5)	99.9858 (20)

5.5 Results

Using the branches obtained above, the weighted mean of the ^{19}Ne half life from the three previous high precision measurements [27, 30, 31], $T_{1/2} = 17.262$ (2)s, the vector part of the statistical phase space factor, $f_V = 98.532$ (58)% [25] and the electron capture fraction, $P_{EC} = 0.101$ [25], we obtain an ft value using the expression

$$f_V t = \frac{f_V T_{1/2}(1 + P_{EC})}{BR} \qquad (5.15)$$
$$f_V t = 1702.8 \text{ (10) s.}$$

Analogous to equation 2.53 one can define a corrected $f_V t$ value after accounting for isospin violating and radiative effects.

$$\mathcal{F}t = f_V t(1 + \delta'_R)(1 + \delta^V_C - \delta^V_{NS}), \qquad (5.16)$$

where δ'_R is a nuclear independent radiative correction and δ^V_C and $\delta_N S^V$ are nuclear structure dependent corrections [25]. Using the result from this experiment, we obtain

$$\mathcal{F}t = 1720.0 \text{ (13)s} \qquad (5.17)$$

A further calculation using the $\mathcal{F}t$ values of superallowed $0^+ \to 0^+$ decays and the approach of Ref. [25] yields

$$\rho = \left[\left(\frac{2\mathcal{F}t^{0^+\to 0^+}}{\mathcal{F}t^{^{19}\mathrm{Ne}}} - 1 \right) \frac{f_V}{f_A} \right]^{1/2} \tag{5.18}$$

where ρ is the Gamow-Teller to Fermi mixing ratio as defined in equation 3.7, f_V/f_A is the ratio of the statistical phase space factors for the vector and axial-vector part of the decay. Finally, one can obtain the Standard Model prediction for the beta asymmetry (A_β) for ^{19}Ne decay using ρ obtained from the above equation and equation 3.8. Our results are shown in Table 5.5 below.

Table 5.5: Comparison between previous work and the result of our work.

Quantity	Previously	Now
$\mathcal{F}t^{^{19}\mathrm{Ne}}$	1718.4 (32) s	1720.0 (13) s
ρ	1.5933 (30)	1.5926 (14)
A_β	-0.04166 (95)	-0.04188 (89)

5.6 Conclusions

In conclusion this work makes the first precision measurement of the $1/2^+ \to 1/2^+$ β decay branch of ^{19}Ne using a radioactive beam. Using available data and our results we obtain a corrected ft value for the decay that is a factor of 2 better than what was known previously. Using this result we obtain a Standard Model prediction of the beta asymmetry for the decay, $A_\beta = -0.04188$ (89) that can be compared to the measured value of $A_\beta = -0.0391$ (14). There is a close to 3σ discrepancy that needs to be investigated further.

References

[1] D. Griffiths. *Introduction to elementary particles.* Wiley, New York, 1987.

[2] D. Piccard. Notes on modern physics and ionization radiation, 2012. `http://www.ohio.edu/people/piccard/radnotes/alphabeta.html`.

[3] K. Krane. *Introductory nuclear physics.* Wiley, New York, 1988.

[4] Triumf.ca. Research facilities — triumf : Canada's national laboratory for particle and nuclear physics, 2016. Available at `http://www.triumf.ca/research-program/research-facilities`.

[5] C. Patrignani et al. Rev. Part. Phys. *Chin. Phys.*, C40(10):100001, 2016.

[6] S. Bilenky. *Introduction to the Physics of Massive and Mixed Neutrinos.* Springer, 2011.

[7] N. Severijns, M. Beck, and O. Naviliat-Cuncic. Tests of the standard electroweak model in nuclear beta decay. *Rev. Mod. Phys.*, 78(3):991, 2006.

[8] O. Naviliat-Cuncic, T. A. Girard, J. Deutsch, and N. Severijns. Left-right symmetry breaking sensitivity of beta -asymmetry measurements. *J. Phys. G: Nuclear and Particle Physics*, 17(6):919, 1991.

[9] A. S. Carnoy, J. Deutsch, R. Prieels, N. Severijns, and P. A. Quin. Is there an indication for the existence of right-handed weak currents in nuclear beta decay? *J. Phys. G: Nuclear and Particle Physics*, 18(5):823, 1992.

[10] B. R. Holstein and S. B. Treiman. Tests of spontaneous left-right-symmetry breaking. *Phys. Rev. D*, 16(7):2369–2372, 1977.

[11] F. P. Calaprice, S. J. Freedman, W. C. Mead, and H. C. Vantine. Experimental study of weak magnetism and second-class interaction effects in the β decay of polarized ^{19}Ne. *Phys. Rev. Lett.*, 35(23):1566, 1975.

[12] B. R. Martin and G. Shaw. *Particle physics*. John Wiley and Sons, 3rd edition edition, 1995.

[13] W. Greiner and B. Müller. *Gauge theory of weak interactions*. Springer Science & Business Media, 2009.

[14] T. D. Lee and C.N. Yang. Question of parity conservation in weak interactions. *Phys. Rev.*, 104(1):254, 1956.

[15] C. S. Wu et al. Experimental test of parity conservation in beta decay. *Phys. Rev.*, 105(4):1413, 1957.

[16] L. Grodzins M. Goldhaber and A. W. Sunyar. Helicity of neutrinos. *Physical Review*, 109(3):1015, 1958.

[17] H. Frauenfelder and E. M. Henley. *Subatomic Physics*. Pearson, 2nd edition, 1991.

[18] H. Georgi and S. L. Glashow. Unity of all elementary-particle forces. *Phys. Rev. Lett.*, 32(8):438, 1974.

[19] R. P. Feynman and M. Gell-Mann. Theory of the fermi interaction. *Phys. Rev.*, 109(1):193, 1958.

[20] J. C. Hardy and I. S. Towner. Superallowed $0^+ \rightarrow 0^+$ nuclear β decays: 2014 critical survey, with precise results for v_{ud} and ckm unitarity. *Phys. Rev. C*, 91(2):025501, 2015.

[21] M. A. B. Bég, R. V. Budny, R. Mohapatra, and A. Sirlin. Manifest left-right symmetry and its experimental consequences. *Phys. Rev. Lett.*, 38(22):1252–1255, 1977.

[22] N. Severijns. Weak interaction studies by precision experiments in nuclear beta decay. In *The Euroschool Lectures on Physics with Exotic Beams, Vol. I*, pages 339–381. Springer, 2004.

[23] J. D. Jackson, S. B. Treiman, and H. W. Wyld. Possible tests of time reversal invariance in beta decay. *Phys. Rev.*, 106(3):517–521, 1957.

[24] J. D. Jackson, S. B. Treiman, and H. W. Wyld. Coulomb corrections in allowed beta transitions. *Nucl. Phys.*, 4:206–212, 1957.

[25] N. Severijns, M. Tandecki, T. Phalet, and I. S. Towner. $\mathcal{F}t$ values of the $t = 1/2$ mirror β transitions. *Phys. Rev. C*, 78(5):055501, 2008.

[26] O. Naviliat-Cuncic and N. Severijns. Test of the conserved vector current hypothesis in t= 1/2 mirror transitions and new determination of $|v_{ud}|$. *Phys. Rev. Lett.*, 102(14):142302, 2009.

[27] S. Triambak et al. High-precision measurement of the ^{19}Ne half-life and implications for right-handed weak currents. *Phys. Rev. Lett.*, 109(4):042301, 2012.

[28] W. Geithner et al. Masses and charge radii of ne 17–22 and the two-proton-halo candidate ^{17}ne. *Phys. Rev. Lett.*, 101(25):252502, 2008.

[29] W. Bambynek et al. Orbital electron capture by the nucleus. *Rev. Mod. Phys.*, 49(1):77, 1977.

[30] P. Ujić et al. Search for superscreening effects in a superconductor. *Phys. Rev. Lett.*, 110(3):032501, 2013.

[31] L. J. Broussard et al. Measurement of the half-life of the t= 1/2 mirror decay of ne 19 and its implication on physics beyond the standard model. *Phys. Rev. Lett.*, 112(21):212301, 2014.

[32] E. R. J. Saettler, F. P. Calaprice, A. L. Hallin, and M. M. Lowry. Beta asymmetry of the first forbidden $1/2^+ \rightarrow 1/2^-$ transition in ^{19}Ne and its relationship to the parity nonconserving nucleon-nucleon interaction. *Phys. Rev. C*, 48(6):3069–3077, 1993.

[33] E. G. Adelberger, M. M. Hindi, C. D. Hoyle, H. E. Swanson, and R. D. Von Lintig. $\frac{1}{2}^+ \to \frac{1}{2}^-$ beta decay of ^{19}Ne and the parity nonconserving NN force. *Phys. Rev. C*, 24:313–316, 1981.

[34] P. Bricault. Status report of the radioactive ion beam production at triumf (invited). *Rev. Sci. Instrum.*, 77(3):03A710, 2006.

[35] C. Geppert et al. Resonance ionization laser ion source - off-line tests at triumf. *Nucl. Phys. A*, 746:631 – 634, 2004.

[36] A.B Garnsworthy. Exotic nuclei studied with the 8pi spectrometer at triumf. In *EPJ Web of Conferences*, volume 93, page 01032. EDP Sciences, 2015.

[37] P. E. Garrett et al. Far from easyspectroscopy with the 8π and griffin spectrometers at triumf-isac. In *J. Phys. : Conference Series*, volume 639, page 012006. IOP Publishing, 2015.

[38] Evaluated Nuclear Structure Data File. National nuclear data center (nndc). *Brookhaven National Laboratory*, 2005.

[39] P. Finlay. *High-Precision Half-Life and Branching-Ratio Measurements for the Superallowed Beta+ Emitter 26Alm*. PhD thesis, 2012.

[40] F. Salvat, J. M. Fernández-Varea, and J. Sempau. Penelope-2008: A code system for monte carlo simulation of electron and photon transport. In *Workshop proceedings*, volume 6416, 2008.

[41] S. A. Teukolsky W. H. Press, B. P. Flannery and W. T. Vetterling. *Numerical Recipes in C: The art of Scientific Computing*. Cambridge University Press, second edition, 1992.

[42] S. Triambak. *The isobaric multiplet mass equation and ft value of the 0+ → 0+ Fermi transition in 32Ar: Two tests of isospin symmetry breaking*. PhD thesis, University of Notre Dame, 2007.